REMMA

Research in ElectroMagnetic
Medical Applications

BOOK OF ABSTRACTS

3rd Student Conference
Research in ElectroMagnetic Medical Applications
Chocen, Czech Republic
8-10 September 2025

Conference Committee

prof. Dr.-Ing. Jan Vrba, M.Sc., Chairman of the Organizing Committee

Email: jan.vrba@fbmi.cvut.cz

doc. Ing. David Vrba, Ph.D., Vice-Chairman of the Organising Committee

Email: david.vrba@fbmi.cvut.cz

Ing. Tomas Pokorny, Ph.D., Main organizer of the REMMA conference

Email: jan.vrba@fbmi.cvut.cz

Ing. Tomas Drizdal, Ph.D., Expert speech and presentation

Email: tomas.drizdal@fbmi.cvut.cz

Editor of the proceedings: Tomas Pokorny

Published in September 2025

The proceedings are available in electronic form at bioem.fbmi.cvut.cz

Acknowledgements

The REMMA conference was supported by the CTU in Prague, project number SVK 58/25/F7 of the Student Grant Competition of the CTU in Prague.


REMMA
STUDENT CONFERENCE
Research in ElectroMagnetic Medical Applications
Czech Technical University in Prague
Faculty of Biomedical Engineering
Splávek


REMMA
Certificate
REMMA
Certificate
REMMA
Certificate

Reconstruction of dielectric parameter change caused by stroke for realistic human head phantom

K. Nouzova[1], T. Pokorny[1] and J. Vrba[1]

[1]Faculty of Biomedical Engineering, CTU in Prague, Czech Republic

Abstract—This study investigates microwave imaging for reconstructing dielectric parameter changes caused by stroke. A realistic multilayer head phantom was created, and scattering parameters were obtained for different stroke sizes and positions using an experimental microwave imaging system. Reconstructions performed with the Born approximation and truncated singular value decomposition demonstrated potential for estimating stroke size, supporting rapid stroke diagnosis.

1. INTRODUCTION

Microwave imaging is being investigated as a portable, inexpensive alternative to MRI and CT for rapid stroke diagnosis [1],[2]. Stroke is a leading cause of death and disability [3], with incidence rising worldwide [4]. Realistic head phantoms allow safe testing of microwave imaging systems, and reconstructions can be performed using Born approximation with truncated singular value decomposition [5],[6].

2. METHODS

Dielectric parameters were measured using a coaxial probe and vector analyzer. The scalp was made from a mixture of polyurethane, conductive carbon black and graphite powders. The skull was made from conductive ABS filament, while the brain was simulated by porcine brains. Stroke phantoms were prepared from water-based mixtures (water, isopropyl alcohol, sodium chloride). Scattering parameters were measured for three stroke sizes and ten positions for both ischemic and hemorrhagic strokes. The influence of the truncation coefficient (Figure 2), stroke size (Figure 3), and position on reconstruction accuracy were investigated.

3. RESULTS

The created head phantom consisted of scalp, skull, and brain layers (Figure 1). Reconstructions for multiple stroke sizes and positions showed the best performance with absolute values of complex permittivity.

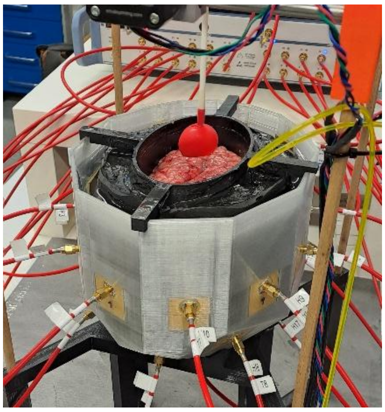

Figure 1. Head phantom in microwave imaging system, composed of polyurethane, ABS, and porcine brains. Stroke phantom in a latex balloon is positioned using a sliding system.

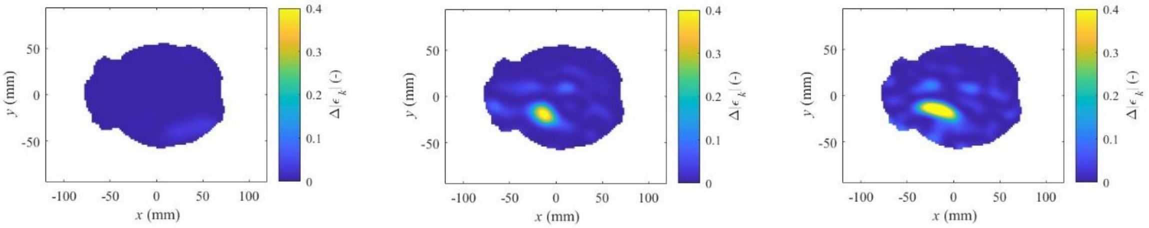

TSVD=10 TSVD=170 TSVD=250

Figure 2. Reconstructions of dielectric parameter changes (absolute value of complex permittivity) for truncation coefficients 10–250, hemorrhagic stroke 33 ml.

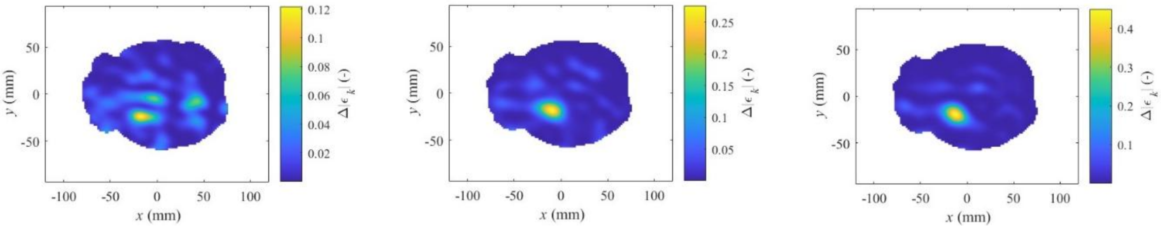

a) b) c)

Figure 3. Reconstructions of dielectric parameter changes (absolute value of complex permittivity) with truncation coefficient 170 for hemorrhagic stroke phantoms of 5 ml (a), 15 ml (b), and 33 ml (c).

4. DISCUSSION

The developed realistic human head phantom enables repeated use for testing microwave imaging systems. Porcine brains, applied here for the first time, proved suitable for creating a brain phantom. The optimal truncation coefficient for reconstruction was identified as 170. Stroke size was not determined directly by the size of the affected area but rather by the dielectric contrast, which increased with stroke volume. Measurement-related shifts of porcine brain tissue limited accuracy in reconstruction for some stroke positions.

5. CONCLUSION

Scattering parameters were measured on a realistic human head phantom using an experimental microwave imaging system. Reconstructions of changes in dielectric parameters caused by stroke performed using Born approximation with truncated singular value decomposition confirm its potential use for determining the location and size of stroke.

ACKNOWLEDGMENT

This work was supported by the Grant Agency of the Czech Technical University in Prague under Grant SGS23/200/OHK4/3T/17, Microwave Imaging Methods for Medical Applications.

REFERENCES

[1] Fhager A., Candefjord S., Elam M., and Persson M., “Microwave Diagnostics Ahead: Saving Time and the Lives of Trauma and Stroke Patients,” *IEEE Microwave Magazine*, vol. 19, no. 3, pp. 78–90, May 2018, doi: 10.1109/MMM.2018.2801646.

[2] Rodriguez-Duarte D. O. *et al.*, “Experimental Validation of a Microwave System for Brain Stroke 3-D Imaging,” *Diagnostics*, vol. 11, no. 7, Art. no. 7, Jul. 2021, doi: 10.3390/diagnostics11071232.

[3] Valery L Feigin *et al.*, “World Stroke Organization: Global Stroke Fact Sheet 2025” Accessed: Apr. 25, 2025. [Online]. Available: https://journals.sagepub.com/doi/10.1177/17474930241308142

[4] Owolabi M. O., Thrift A. G., Mahal A., Ishida M, Martins S., and et al., “Primary stroke prevention worldwide: translating evidence into action,” *The Lancet Public Health*, vol. 7, no. 1, pp. e74–e85, Jan. 2022, doi: 10.1016/S2468-2667(21)00230-9.

[5] Origlia C. *et al.*, “Experimental Validation of a Microwave Scanner for Brain Stroke Monitoring in Realistic Head Models,” in *2023 IEEE International Symposium on Antennas and Propagation and USNC-URSI Radio Science Meeting (USNC-URSI)*, Jul. 2023, pp. 509–510. doi: 10.1109/USNC-URSI52151.2023.10237424.

[6] Rodriguez-Duarte D. O., Origlia C., Vasquez J. A. T., and et al., “Experimental Assessment of Real-Time Brain Stroke Monitoring via a Microwave Imaging Scanner,” *IEEE Open Journal of Antennas and Propagation*, vol. 3, pp. 824–835, 2022, doi: 10.1109/OJAP.2022.3192884.

Antenna Element for Pediatric Regional Hyperthermia System

J. Mach[1]

[1]Czech Technical University in Prague, Faculty of Biomedical Engineering,
Kladno, Czech Republic

Abstract—This paper presents the design, manufacturing, and verification of an innovative antenna element for regional hyperthermia in pediatrics. The study focuses on the development of a dielectric parabolic reflector antenna (DiPRA) operating at 200 MHz, designed for hyperthermic treatment in the abdominal and pelvic regions in children. Three candidate antennas as a patch, Yagi-Uda, and DiPRA were simulated in Sim4Life and analyzed in terms of reflection coefficient and specific absorption rate (SAR) distribution. The DiPRA antenna has shown excellent directivity and homogeneous SAR focusing compared to the other designs. The prototype was manufactured using a dipole with a printed circuit board integrated into a 3D-printed parabolic reflector filled with deionized water. Experimental verification using the cSAR3D phantom confirmed the simulation results and achieved a reflection coefficient of -21 dB at 200 MHz. The results highlight the potential of the DiPRA antenna for the safe and effective delivery of hyperthermia in pediatric oncology, addressing the limitations of systems designed for adults and emphasizing improved treatment precision and safety.

1. INTRODUCTION

Pediatric oncology requires therapeutic approaches that not only improve survival but also minimize late side effects of chemotherapy (CHT) and radiotherapy (RT). Regional hyperthermia (RHT) appears to be a promising adjunctive method, as mild heating (40–44 °C) increases tumor sensitivity to CHT or RT and stimulate the antitumor immune response[1–4]. However, current RHT systems are primarily designed for adults, and their size and power are not suitable for children [5, 6]. To address this limitation, this paper focuses on the design and experimental verification of a new antenna element for a pediatric RHT system targeting abdominal and pelvic tumors.

2. METHODS

Based on a review of the literature, three types of antennas were considered: patch antenna, Yagi-Uda antenna, and dielectric parabolic reflector antenna (DiPRA). The models were created in Sim4Life and tuned to 200 MHz, a frequency suitable for pediatric RHT [5]. The simulations included the distribution of the reflection coefficient (S11) and specific absorption rate (SAR) in a phantom equivalent to tissue with a water bolus. Based on the simulation results, the DiPRA antenna was selected. The antenna was then manufactured using a PCB dipole fitted in a 3D-printed parabolic reflector filled with deionized water. Experimental validation of S11 was performed on the cSAR3D system using a spectrum analyzer.

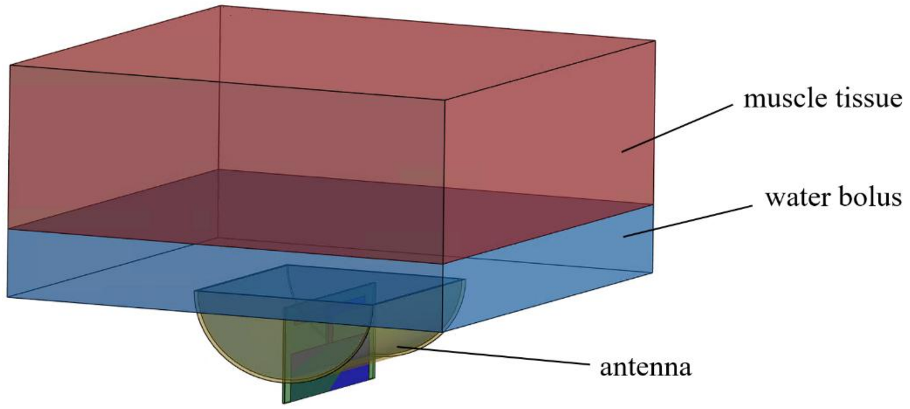

Figure 1. Arrangement of the antenna element (DiPRA) relative to the tissue phantom and water bolus.

3. RESULTS

The simulation results showed that all three antennas achieved the target value of S11 < -10 dB. The patch antenna achieved the lowest reflection coefficient (–32 dB), while the DiPRA achieved a value of –22 dB. However, DiPRA demonstrated better SAR homogeneity and deeper focus. The manufactured DiPRA antenna achieved an experimental reflection coefficient of –21 dB at 200 MHz.

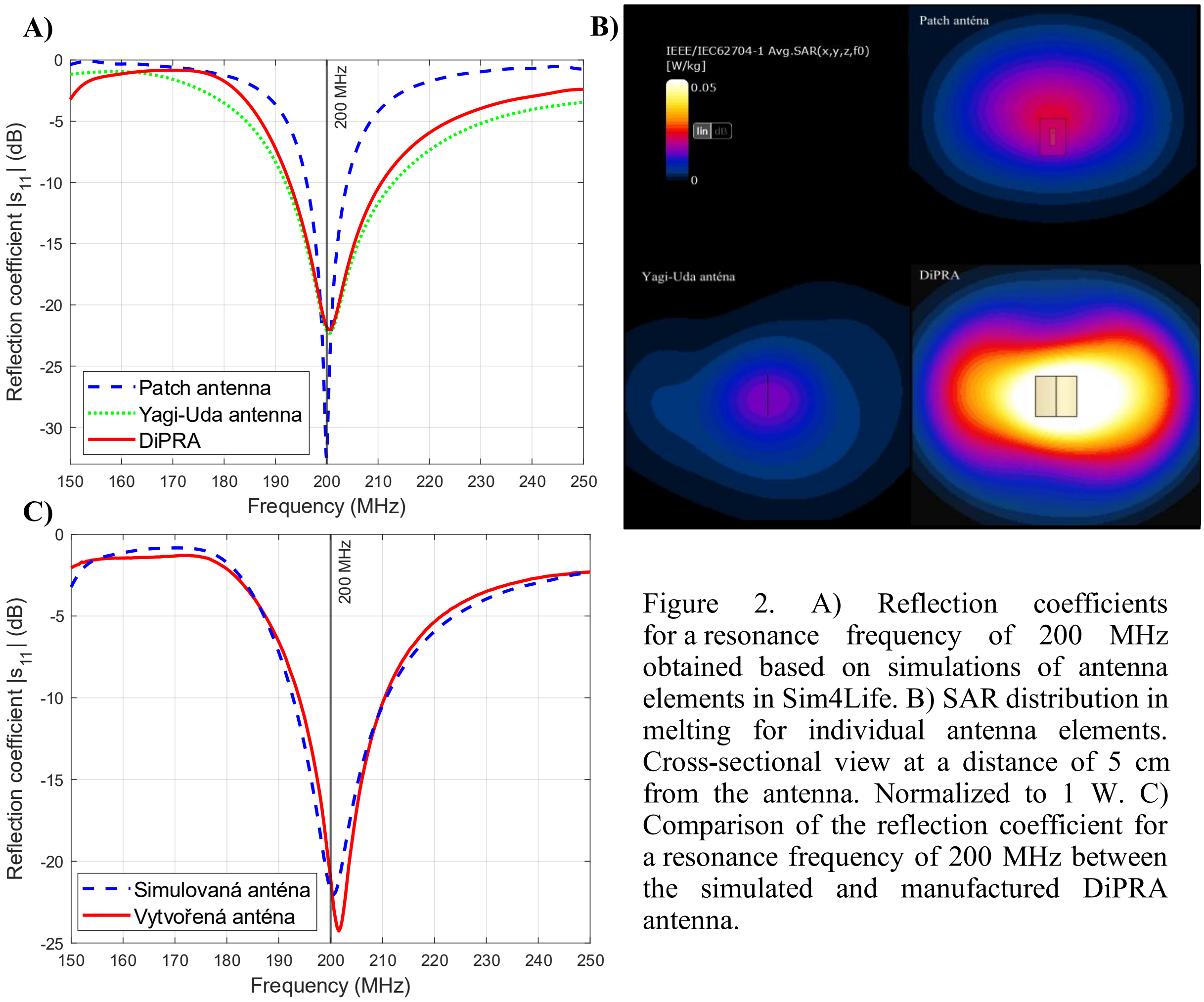

Figure 2. A) Reflection coefficients for a resonance frequency of 200 MHz obtained based on simulations of antenna elements in Sim4Life. B) SAR distribution in melting for individual antenna elements. Cross-sectional view at a distance of 5 cm from the antenna. Normalized to 1 W. C) Comparison of the reflection coefficient for a resonance frequency of 200 MHz between the simulated and manufactured DiPRA antenna.

4. DISCUSSION

The main outcome of this work is a designed and manufactured antenna with an operating frequency of 200 MHz for the RHT system, intended for the treatment of pediatric oncology patients in the abdominal and pelvic areas. Although patch and Yagi-Uda antennas provided good matching, the DiPRA antenna proved to be the most suitable for pediatric applications due to its strong directivity. Although patch and Yagi-Uda antennas provided good impedance matching, the DiPRA antenna proved to be the most suitable for pediatric applications due to its strong directivity, homogeneous SAR distribution, and compact size. The design ensures a reduced risk of surface hotspots, which is particularly important in children with smaller anatomical structures and higher sensitivity to thermal loading. Future verification on realistic tissue phantoms and integration with a power amplifier is necessary.

5. CONCLUSION

A new 200 MHz DiPRA antenna for use in pediatric regional hyperthermia systems has been successfully designed, manufactured, and validated. The antenna has shown promising performance in terms of SAR distribution and reflection coefficient, indicating its potential for safe and effective use in the treatment of abdominal and pelvic hyperthermia in pediatric patients.

REFERENCES

[1] TYDINGS, Caitlin, Karun V. SHARMA, AeRang KIM a Pavel S. YARMOLENKO. Emerging hyperthermia applications for pediatric oncology. *Advanced Drug Delivery Reviews* [online]. 2020, **163–164**, 157–167 [vid. 2023-07-30]. ISSN 0169409X. Dostupné z: doi:10.1016/j.addr.2020.10.016

[2] WESSALOWSKI, Rüdiger, Heidi KRUCK, Hildegard PAPE, Thomas KAHN, Reinhart WILLERS a Ulrich GÖBEL. Hyperthermia for the treatment of patients with malignant germ cell tumors. *Cancer* [online]. 1998, **82**(4), 793–800 [vid. 2024-02-23]. ISSN 1097-0142. Dostupné z: doi:10.1002/(SICI)1097-0142(19980215)82:4<793::AID-CNCR24>3.0.CO;2-S

[3] WESSALOWSKI, Rüdiger, Dominik T. SCHNEIDER, Oliver MILS, Verena FRIEMANN, Olga KYRILLOPOULOU, Jörg SCHAPER, Christiane MATUSCHEK, Karin ROTHE, Ivo LEUSCHNER, Reinhart WILLERS, Stefan SCHÖNBERGER, Ulrich GÖBEL a Gabriele CALAMINUS. Regional deep hyperthermia for salvage treatment of children and adolescents with refractory or recurrent non-testicular malignant germ-cell tumours: an open-label, non-randomised, single-institution, phase 2 study. *The Lancet Oncology* [online]. 2013, **14**(9), 843–852 [vid. 2024-01-02]. ISSN 1470-2045, 1474-5488. Dostupné z: doi:10.1016/S1470-2045(13)70271-7

[4] KOK, H. Petra, Erik N. K. CRESSMAN, Wim CEELEN, Christopher L. BRACE, Robert IVKOV, Holger GRÜLL, Gail TER HAAR, Peter WUST a Johannes CREZEE. Heating technology for malignant tumors: a review. *International Journal of Hyperthermia* [online]. 2020, **37**(1), 711–741 [vid. 2023-03-24]. ISSN 0265-6736. Dostupné z: doi:10.1080/02656736.2020.1779357

[5] MACH, Jakub. *Regionální hypertermický systém pro léčbu dětských onkologických pacientů* [online]. Kladno, 2024 [vid. 2025-06-04]. České vysoké učení technické v Praze.

Vypočetní a informační centrum. Dostupné z: https://dspace.cvut.cz/handle/10467/119165

[6] SEIFERT, Georg, Volker BUDACH, Ulrich KEILHOLZ, Peter WUST, Angelika EGGERT a Pirus GHADJAR. Regional hyperthermia combined with chemotherapy in paediatric, adolescent and young adult patients: current and future perspectives. *Radiation Oncology* [online]. 2016, **11**(1), 65 [vid. 2023-12-08]. ISSN 1748-717X. Dostupné z: doi:10.1186/s13014-016-0639-1

Optimization of the stroke phantom positioning system

Michal Karel

Faculty of Biomedical Engineering, Czech Technical University in Prague, Czech Republic

Abstract — Cerebrovascular accident (stroke) is one of the leading causes of death and long-term disability worldwide [1]. Recent developments in microwave imaging have shown potential for rapid prehospital stroke diagnostics [2]. However, the effectiveness of machine learning algorithms used for classification strongly depends on the availability of large and diverse experimental datasets. This work presents the design and implementation of an optimized automated positioning system (APS) for stroke phantoms, enabling the acquisition of extensive datasets for training and testing classification algorithms. The system provides precise positioning in three spatial axes and introduces a novel mechanism for automated lesion size variation. This innovation overcomes key limitations of previous experimental setups and significantly accelerates data collection.

1. INTRODUCTION

Stroke diagnostics currently relies mainly on CT and MRI, which are limited in prehospital use due to transport delays and cost [3]. Microwave imaging offers a portable, safe, and fast alternative. Nevertheless, the development of reliable machine learning models requires high-quality datasets, which are difficult to obtain from clinical practice [2]. Measurement on realistic phantoms represents an essential step, but current positioning systems allow only limited variability.

2. METHODS

The APS was developed by extending a previously published 2D positioning system [4] to 3D motion (X, Y, Z axes) and integrating an actuator for automated lesion size control. Four NEMA 17 stepper motors controlled by Arduino UNO with CNC shield and A4988 drivers enable precise movements. MATLAB scripts were implemented to synchronize APS control with a vector network analyzer (VNA) and to automate data acquisition.

3. RESULTS

The system enables automated measurement of stroke phantoms filled with dielectric liquids simulating ischemic and hemorrhagic strokes. A dataset of 1600 S-matrices was generated during 33 hours of continuous measurement, including three lesion sizes (20, 30, and 40 mm) at multiple spatial positions. This represents a substantial increase compared to previously published datasets, which typically include only tens or hundreds of measurements.

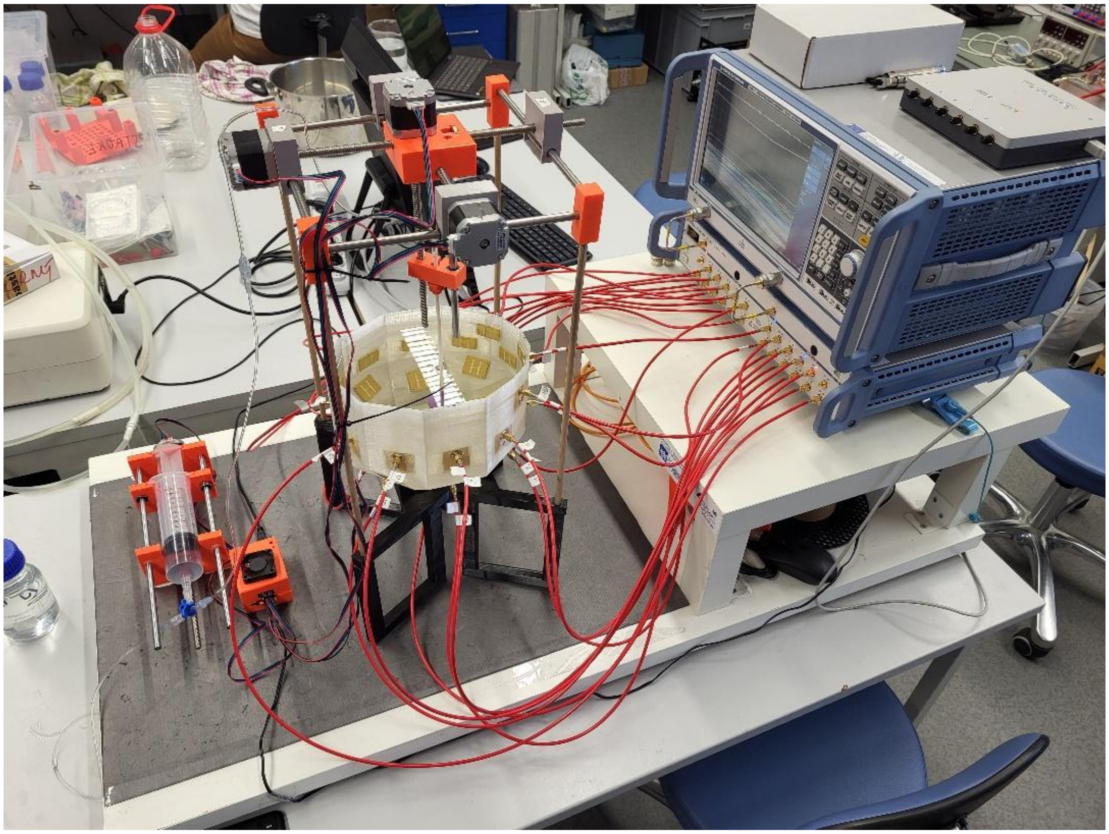

Figure 1: The entire system during measurement.

4. DISCUSSION

The developed APS provides high flexibility and reproducibility, ensuring systematic variation of lesion size and position. Compared to other experimental systems [5; 6], it enables significantly larger and more diverse datasets, which are crucial for machine learning-based classification of stroke types.

5. CONCLUSION

The optimized positioning system enabled the acquisition of 1600 S-matrices within 33 hours, covering multiple lesion sizes and positions. This large and diverse dataset provides a solid basis for training machine learning algorithms for stroke classification. It represents a significant step toward the development of robust machine learning models for stroke classification in microwave imaging.

REFERENCES

[1] FEIGIN, Valery L, Michael BRAININ, Bo NORRVING, et al. World Stroke Organization (WSO): Global Stroke Fact Sheet 2022. International Journal of Stroke [online]. 2022, 17(1), 18-29 [cit. 2024-05-02]. ISSN 1747-4930. Dostupné z: doi:10.1177/17474930211065917

[2] KARADIMA, Olympia, Raquel C. CONCEICAO a Panagiotis KOSMAS. Differentiation of brain stroke type by using microwave-based machine learning classification. 2021 International Conference on Electromagnetics in Advanced Applications (ICEAA) [online]. IEEE, 2021, 2021-8-9, 185-185 [cit. 2023-04-07]. ISBN 978-1-6654-1386-2. Dostupné z: doi:10.1109/ICEAA52647.2021.9539740

[3] MARIANO, Valeria, Jorge A. TOBON VASQUEZ, Mario R. CASU a Francesca VIPIANA. Brain Stroke Classification via Machine Learning Algorithms Trained with a Linearized Scattering Operator. Diagnostics [online]. 2023, 13(1) [cit. 2025-05-27]. ISSN 2075-4418. Dostupné z: doi:10.3390/diagnostics13010023

[4] POKORNY, Tomas, Tomas DRIZDAL, Marek NOVAK a Jan VRBA. Automated, Reproducible, and Reconfigurable Human Head Phantom for Experimental Testing of Microwave Systems for Stroke Classification. International Journal of Imaging Systems and Technology [online]. 2024, 34(6) [cit. 2025-06-16]. ISSN 0899-9457. Dostupné z: doi:10.1002/ima.23200

[5] TOBON VASQUEZ, Jorge A., Rosa SCAPATICCI, Giovanna TURVANI, et al. A Prototype Microwave System for 3D Brain Stroke Imaging. Sensors [online]. 2020, 20(9) [cit. 2023-05-16]. ISSN 1424-8220. Dostupné z: doi:10.3390/s20092607

[6] CUCCARO, Antonio, Angela DELL'AVERSANO, Bruno BASILE, Maria Antonia MAISTO a Raffaele SOLIMENE. Subcranial Encephalic Temnograph-Shaped Helmet for Brain Stroke Monitoring. Sensors [online]. 2024, 24(9) [cit. 2025-03-04]. ISSN 1424-8220. Dostupné z: doi:10.3390/s24092887

Effect of changes in GABAergic inhibition on the development of tinnitus

Klára Kozelková[1]

[1]Czech Technical University in Prague, Faculty of Biomedical Engineering, nám. Sítná 3105, 272 01 Kladno, Czech Republic

Abstract

Tinnitus is perceived as an auditory sensation without an external acoustic source. It can be very unpleasant and patients face many consequences such as insomnia, depression or even thoughts of suicide. The aim of this study was to verify and evaluate by the acoustic startle response method the presence of tinnitus in animal models and to compare the susceptibility to its development between two groups of mice. The difference between the groups of animals was the absence of the KCTD16 protein in one of them. The other group was a control and was named C57 (WT). Tinnitus was assessed using the Gap Prepulse Inhibition of the Acoustic Startle (GPIAS) method. The accompanying DPOAE (Distortion Product Otoacoustic Emissions) and ABR (Auditory Brainstem Response) methods contributed to a detailed assessment of auditory function and the extent of impairment after deafening. Deafening was performed by exposing animals to noise. Measurements resulted in a differential susceptibility to develop tinnitus at higher frequencies in mice lacking the KCTD16 protein.

1. INTRODUCTION

Tinnitus is the perception of sound without an external source, often described as ringing, buzzing, or popping in the ears. It typically follows hearing loss caused by noise exposure, ototoxic drugs, infections, injuries, or genetic predisposition. Tinnitus can severely impact mental health and, in extreme cases, lead to depression or suicide. [1]

Neural correlates include increased spontaneous activity and synchrony of auditory neurons, likely due to reduced GABAergic inhibition. GABA-B receptors, composed of GB1/GB2 and KCTD auxiliary subunits, regulate neuronal excitability. KCTD proteins modulate receptor surface expression and kinetics. [2]

2. METHODS

GPIAS (Gap Pre-pulse Inhibition of Acoustic Startle):

Tinnitus was assessed using the GPIAS method. Mice were placed in a soundproof chamber in wire cages on a pressure-sensitive platform. The startle response to acoustic stimuli was measured with and without a brief silent gap. GPIAS was calculated as:

$$GPIAS\,(\%) = (1 - [ASR\_gap \,/\, ASR\_no - gap]) \cdot 100. \qquad (1)$$

DPOAE (Distortion Product Otoacoustic Emissions):

Outer hair cell function was evaluated in anesthetized mice. DPOAEs were recorded via a microphone probe in the ear canal in response to two primary tones ($f2$ = 4–40 kHz, $f2/f1$ = 1.21, $L1/L2$ = 70/65 dB SPL).

Figure 1 Demonstration of a mouse during DPOAE auditory emission measurement

ABR (Auditory Brainstem Responses):

ABRs were recorded from anesthetized mice using subcutaneous electrodes. Sound stimuli (clicks and tones from 0–100 dB SPL) were presented in free-field conditions to determine hearing thresholds.

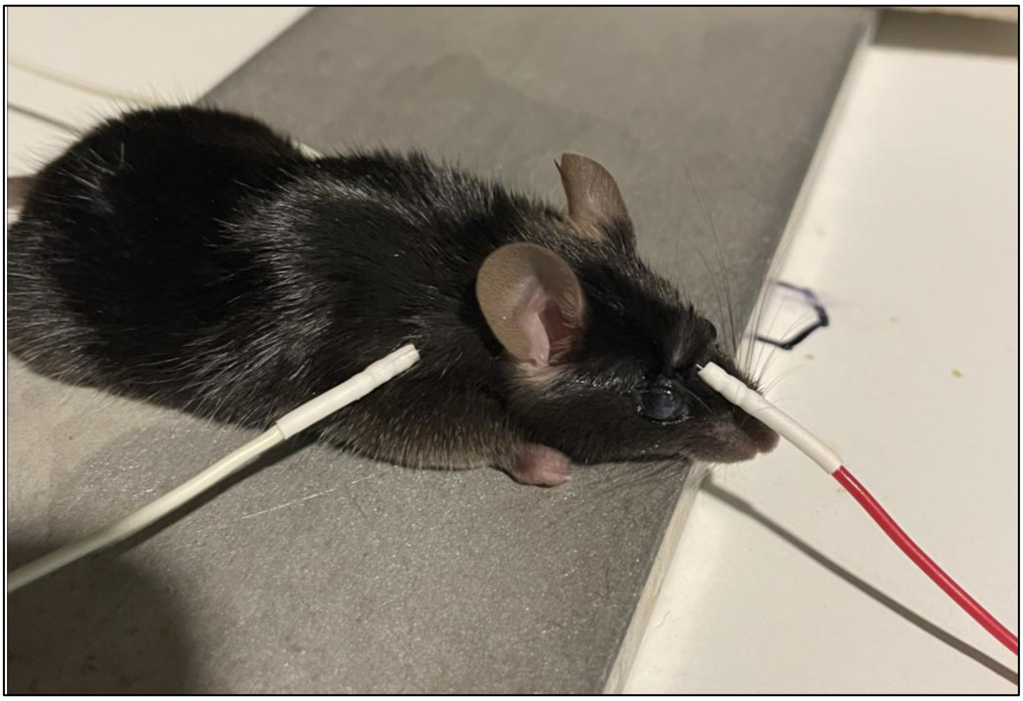

Figure 2 Demonstration of needle electrode insertion

Noise Exposure:

Tinnitus was induced by exposing anesthetized mice to 10 kHz narrowband noise at 116 dB SPL for 1 hour.

3. RESULTS

The following results show differences between the two groups of mice in their responses to acoustic stimuli. The first three graphs are a comparison of GPIAS at 4, 10 and 16 kHz NBN before and after noise exposure.

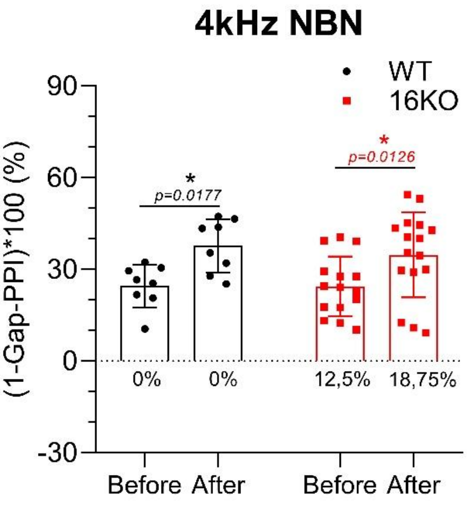

Figure 3 GPIAS results, background noise at 4 kHz

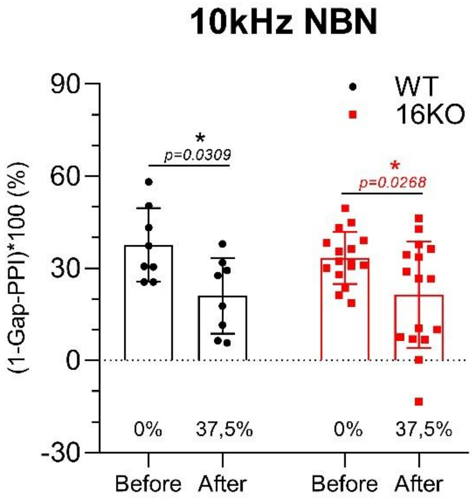

Figure 4 GPIAS results, background noise at 10 kHz

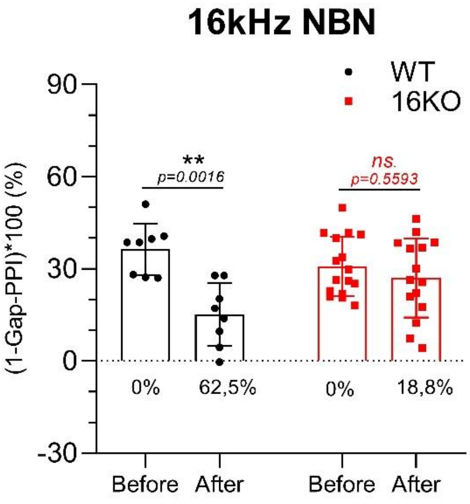

Figure 5 GPIAS results, background noise at 16 kHz

The second part of the results shows the difference between groups in DPOAE at higher frequencies. This difference was also confirmed for the DPOAE in response to the 8 kHz sound. *(NE = noise exposure)*

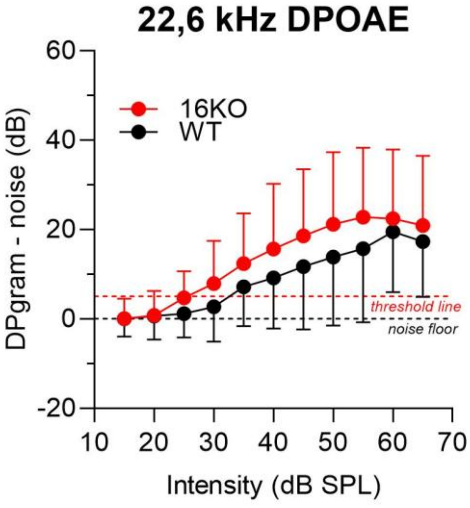

Figure 6 DPOAE at 22,6 kHz, before NE

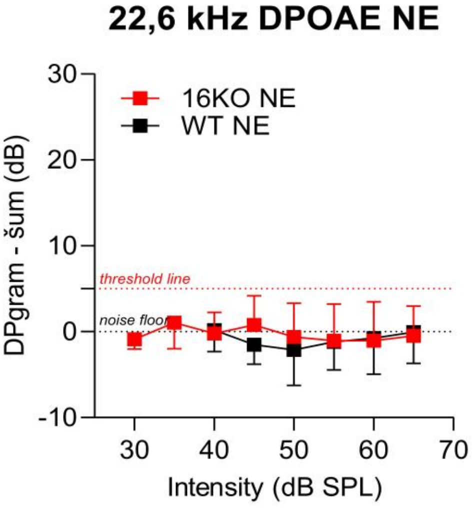

Figure 7 DPOAE at 22,6 kHz, after NE

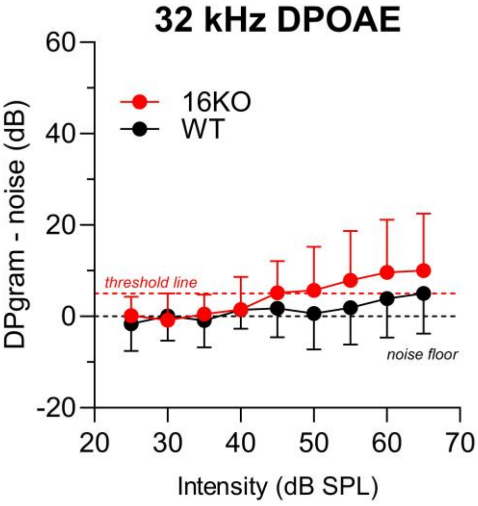

Figure 8 DPOAE at 32 kHz, before NE

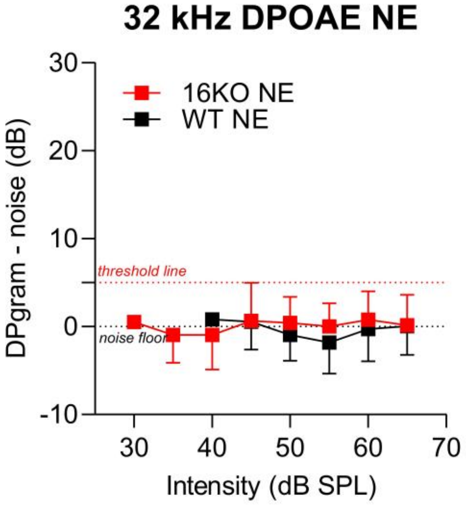

Figure 9 DPOAE at 32 kHz, after NE

Elevation of hearing thresholds after noise exposure of animals was also observed using the DPOAE method. The arrows in the graph indicate that the response at a given frequency was not noticeable even at 70 dB. This intensity required to achieve a response is no longer increased due to the risk of further potential damage to the animal's hearing.

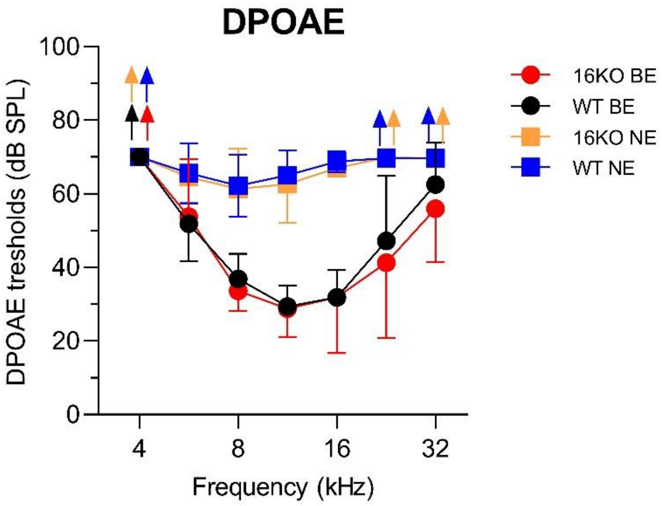

Figure 10 Elevation of hearing thresholds after noise exposure

Further confirmation of mouse deafening is the shift in auditory thresholds shown by the ABR method.

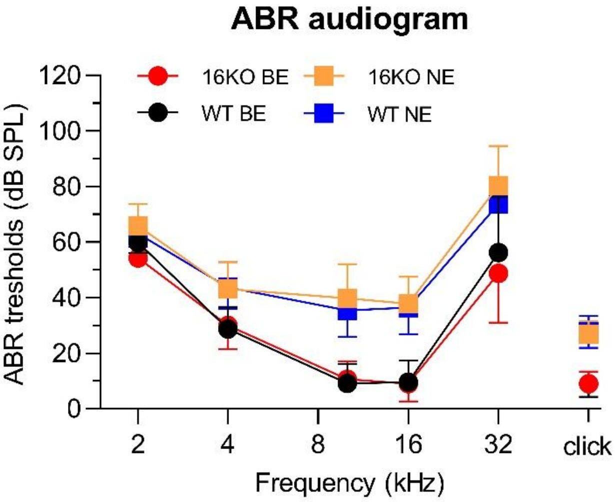

Figure 11 ABR audiogram results before and after NE

4. DISCUSSION

Tinnitus was assessed in two mouse groups using the GPIAS method. The 16KO group, lacking the KCTD16 protein, showed lower susceptibility to tinnitus after noise exposure compared to the WT group. ABR threshold shifts at low frequencies were also more pronounced in 16KO mice after deafening.

GPIAS was essential in detecting tinnitus both before and after acoustic trauma, revealing differences in inhibitory processing. **DPOAE** and **ABR** confirmed hearing loss, evident by reduced amplitudes and threshold elevations.

Tinnitus Findings:

Tinnitus was detected in 56% of 16KO mice and 75% of WT mice post-exposure. At 16 kHz, only 3 of 16KO mice developed tinnitus versus 5 of 8 WT mice. These results suggest a protective role of KCTD16 in processing high-frequency sounds.

Hearing Loss:

At 8 kHz, significant intra-group differences were observed after noise exposure. At higher frequencies (22.6–32 kHz), amplitude drops were evident across both groups, indicating hair cell dysfunction. ABR results showed threshold shifts at 4, 10, 16, and 32 kHz in both groups, with additional shifts at 2 kHz in 16KO mice, suggesting greater vulnerability to noise.

5. CONCLUSION

This study confirms that genetic differences between WT and 16KO mice influence their sensitivity to acoustic trauma, tinnitus development, and shifts in auditory thresholds. The GPIAS method was key in detecting tinnitus and identifying inhibitory differences between groups.

Supporting methods, DPOAE and ABR, confirmed hearing loss through reduced otoacoustic emissions and elevated thresholds. Notably, the 16KO group showed lower susceptibility to tinnitus at higher frequencies, suggesting that absence of the KCTD16 protein may enhance GABA-B receptor function.

These findings contribute to a better understanding of how genetic predispositions may shape vulnerability to tinnitus and auditory damage.

ACKNOWLEDGMENT

The author would like to thank her supervisor of this project Ing. Michaela Mrázková for her help with the preparation. Many thanks also to Bc. Štěpánka Suchánková for her training in measurement methods and help with the project results. Furthermore, the author would like to thank Mr. RNDr. Rostislav Tureček, CSc. for explaining the issue and enabling the measurements in cooperation with the Academy of Sciences of the Czech Republic.

REFERENCES

[1] ROBERTS, Larry E., Jos J. EGGERMONT, Donald M. CASPARY, Susan E. SHORE, Jennifer R. MELCHER a James A. KALTENBACH. Ringing Ears: The Neuroscience of Tinnitus: Figure 1. *The Journal of Neuroscience* [online]. 2010, 2010-11-10, **30**(45), 14972-14979 [cit. 2024-11-07]. ISSN 0270-6474. Available from: doi:10.1523/JNEUROSCI.4028-10.2010

[2] TUREČEK, Rostislav, Adolf MELICHAR, Michaela KRÁLÍKOVÁ a Bohdana HRUŠKOVÁ. The role of GABAB receptors in the subcortical pathways of the mammalian auditory system. *Frontiers in Endocrinology* [online]. 2023, 2023-8-11, **14** [cit. 2024-10-30]. ISSN 1664-2392. Available from: doi:10.3389/fendo.2023.1195038

Simulation of an emerging ischemic stroke

A. Dalekorei[1]

[1]Faculty of Biomedical Engineering, Czech Technical University in Prague, Prague, Czech Republic

Abstract—The aim of this project was to simulate the early dielectric response of ischemic brain tissue using controlled liquid phantom and measure it at central frequency 1 GHz. Based on the existing research papers showing a characteristic ~15% drop in relative permittivity and electrical conductivity within the first hour of stroke onset, we composed a mixture that allows to gradually influence dielectric properties via incremental addition to the liquid brain phantom. Two trials have been conducted, using different volume composition of such ingredients as: distilled water, isopropyl alcohol (IPA) and NaCl. Measurements were obtained using SPEAG Dielectric Assessment Kit (DAK 3.5) and processed with a MATLAB script for uncertainty analysis. Mixture Sample 2 was found to be more successful, achieving desired value within volume limit. The results support the potential of this phantom design to model early stroke development and future research application.

1. INTRODUCTION

Stroke, particularly ischemic stroke, remains one of the leading causes of death and disability worldwide [1-4]. Despite preventive strategies, global incidence continues to rise, with notable increases among younger populations [4-5]. The burden is closely linked to lifestyle, diet, and healthcare disparities, while the COVID-19 pandemic further hindered progress [6]. Given its fast progression, early and accurate detection of ischemic stroke is crucial. Conventional imaging modalities such as CT, MRI, and Doppler ultrasonography enable effective diagnosis, yet remain bulky, costly, limited in availability, or invasive [9]. This has motivated research into microwave imaging (MWI), which offers a safe, rapid, and potentially portable diagnostic tool by exploiting the dielectric contrast between healthy and ischemic brain tissue [10-12].

On a technical level, ischemic stroke is caused by thromboembolic blockage of cerebral blood flow, leading to loss of function in the affected brain region [7-8]. During ischemia, dielectric properties of brain tissue decrease significantly reported reductions range from 10% up to 25% depending on conditions [10]. Such shifts form the basis for detection through MWI systems, which are sensitive to changes in permittivity and conductivity.

Recent contributions have explored this concept through three main directions: in vivo dielectric characterization, phantom development, and microwave imaging system validation. In vivo data remain scarce, but a key study [10] measured dielectric properties in pigs during controlled carotid artery occlusion and reperfusion, finding ~10% reduction after 60 minutes of ischemia. Phantom-based studies complement this by providing reproducible testbeds. For example, a Czech group developed multilayer 2.5D head phantoms with anatomically realistic structures, combining polyurethane rubber composites for scalp and skull, liquid mixtures for cerebrospinal fluid, and adjustable brain phantoms [11]. These designs allow embedding of stroke-mimicking lesions and circulatory systems, though long-term dielectric stability remains a limitation. Parallel to this, MWI system prototypes have been validated with anthropomorphic phantoms. One example used 24 printed monopole antennas arranged around a conformal medium and employed advanced calibration to reconstruct stroke lesions across 0.1–10 GHz

[12]. While promising, these setups often rely on simplified or ex vivo models and fixed stroke scenarios, underlining the need for dynamic and reconfigurable approaches.

Microwave systems specifically designed for stroke detection emphasize portability and reproducibility. Antenna arrays, often arranged around head phantoms, operate at ~1 GHz to capture S-parameters reflecting localized dielectric changes [13-18]. To simulate realistic ischemic onset, reconfigurable phantoms with balloon chambers or fluid circulation systems have been proposed, enabling progressive lesion formation [16-17]. Signal analysis methods, including support vector machine (SVM) classification and PCA-based feature extraction, have shown potential in distinguishing early ischemic regions [18]. These findings reinforce the feasibility of MWI as a diagnostic technology but also highlight challenges in phantom stability, biological complexity, and clinical validation.

2. METHODS

This project was designed to simulate the early stages of an ischemic stroke through a controlled drop in the dielectric properties of brain tissue. Previous studies [10], [17] reported ~15% reduction in relative permittivity (ε) and conductivity (σ) within one hour of ischemia, which we used as a reference for developing and validating a phantom-based simulation under controlled conditions [10-11] and [17].

Equipment, materials, and tools

Measurements were performed using the SPEAG Dielectric Assessment Kit (DAK) with a DAKS 3.5 open-ended coaxial probe, operating from 0.2–3 GHz and connected to a Planar R180 Network Analyzer. Samples were evaluated at 1 GHz, a standard frequency for microwave stroke detection [2], [10] and [17-18]. Prior to measurement, temperature was recorded at 24.07 °C, while humidity was assumed from average laboratory conditions (51.2 ± 0.9%). The probe was calibrated with the Open, Short, and Load method using distilled water. During testing, the probe was immersed without air bubbles, cleaned between samples, and measurements were taken in a triangular laboratory beaker.

Liquid phantom design

Liquid phantoms were prepared from distilled water, isopropyl alcohol (IPA), and NaCl, a combination capable of reproducing a wide dielectric range of biological tissues. Individual properties were first measured: water ($\varepsilon \approx 76.5,\ \sigma \approx 0.165\ S/m$), IPA ($\varepsilon \approx 9,\ \sigma \approx 0.3\ S/m$). Water increased permittivity, salt increased conductivity, and IPA reduced both. Using this, experimental mixtures were created to progressively lower dielectric properties. Because syringe volume limited stroke mixtures to 150 ml, additions were made in 10 ml steps, with a two-minute stabilization before recording.

Brain phantom

The base brain phantom consisted of 100 ml of a water–IPA–NaCl mixture, designed to approximate brain tissue at 1 GHz ($\varepsilon \approx 45,\ \sigma \approx 1\ S/m$). Actual prepared values were slightly lower ($\varepsilon \approx 43,\ \sigma \approx 0{,}9\ S/m$) and were adjusted before experiments. This phantom served as the baseline for all trials.

Ischemic stroke progression phantom

Stroke progression was simulated by adding mixtures designed to reduce dielectric properties. The first trial mixture contained 10 ml IPA, 5 ml water, and 0.1 g NaCl; the second, 20 ml IPA, 5 ml water, and 0.1 g NaCl. These were added in 10–15 ml steps, stirred until NaCl dissolved, and stabilized before measurement. Each condition was measured 10 times, and results were exported to Excel.

Mixture evaluations

Data was processed at 1 GHz. MATLAB scripts calculated mean values, uncertainties (A, B, C), and plotted results. The percentage drop was computed as:

$$\Delta x\ (\%) = \frac{x_{measured} \cdot 100\%}{x_{baseline}} - 100\% \tag{1}$$

where Δx is percentage drop of dielectric properties after adding the mixture, $x_{measured}$ is measured values of the dielectric properties and $x_{baseline}$ is values of dielectric properties of the liquid brain at the beginning of the experiment.

Evaluation of samples

Graphs were created showing percentage drops in permittivity and conductivity against added mixture volume. A second-order polynomial trendline highlighted progression and enabled estimation of volumes required for specific reductions (3%, 6%, 9%, 12%, 15%). The aim was to ensure both ε and σ decreased consistently, avoiding divergence, thereby producing a stable and physiologically realistic ischemic phantom for further experiments.

3. RESULTS

We first measured the initial brain phantom, with the results presented in Table 3.1 and Figure 3.1. To simulate the development of an ischemic stroke, where the brain dielectric properties decrease, we gradually added our mixtures and observed the resulting changes in dielectric properties.

The results for two trials are shown in Tables 3.2 and 3.3, and the decrease in dielectric parameters is illustrated in Figures 3.2 and 3.3.

Initial brain phantom

Table 3.1: Mean values of dielectric properties and U_A, U_B, U_C of the liquid brain at 1 GHz

Parameter	**Permittivity**	**Conductivity**
Mean value	45.75	1.08
Uncertainty A	0.00	0.00
Uncertainty B	0.80	0.01
Uncertainty C	1.60	0.02

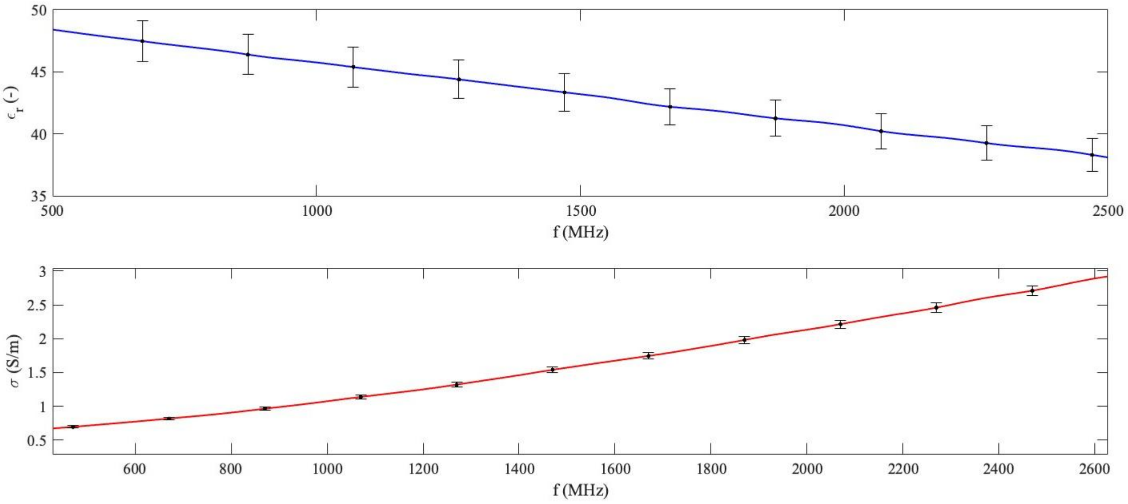

Figure 3.1: Graph representing dielectric properties values of the initial brain phantom at the frequency range 0.5 – 2.5 GHz

Sample 1

Mixture 1 was composed from 10 ml IPA, 5 ml distilled water and 0.1 g salt.

Table 3.2: Effect of added mixture 1on permittivity and conductivity

Mixture volume V (ml)	$\varepsilon_{mean} \pm U_C$ (-)	$\sigma_{mean} \pm U_C$ (S/m)	$\Delta\varepsilon$ (%)	$\Delta\sigma$ (%)
0	45.16 ± 1.58	1.09 ± 0.02	-	-
15	42.93 ± 1.53	1.03 ± 0.02	- 4.94	- 5.77
30	41.29 ± 1.45	0.98 ± 0.01	- 8.57	- 9.65
45	39.89 ± 1.40	0.95 ± 0.01	- 11.67	- 12.86
60	39.02 ± 1.37	0.93 ± 0.01	- 13.59	- 14.85
75	38.27 ± 1.34	0.91 ± 0.01	- 15.26	- 16.42

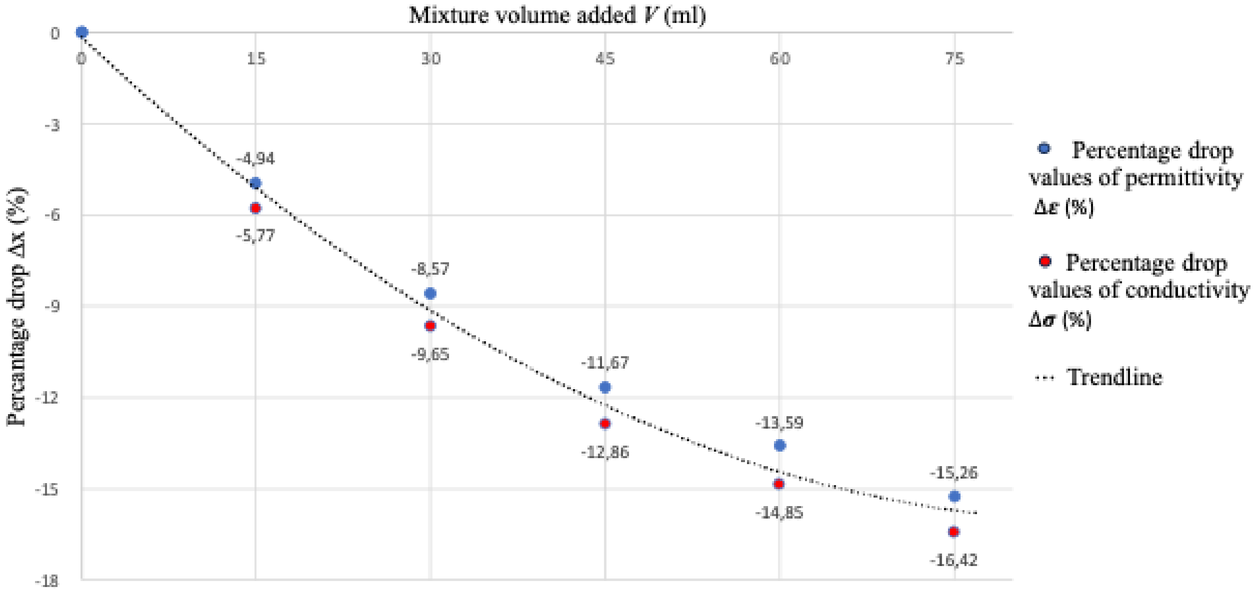

Figure 3.2: Percentage decrease in permittivity and conductivity with increasing volume of mixture added to the initial brain phantom (based on Table 3.2)

Sample 2

Mixture 2 was composed from 20 ml IPA, 5 ml distilled water and 0.1 g salt.

Table 3.3: Effect of added mixture 2 on permittivity and conductivity – Sample 2

Mixture volume V (ml)	$\boldsymbol{\varepsilon_{mean}} \pm \boldsymbol{U_C}$ **(-)**	$\boldsymbol{\sigma_{mean}} \pm \boldsymbol{U_C}$ **(S/m)**	$\boldsymbol{\Delta\varepsilon}$ **(%)**	$\boldsymbol{\Delta\sigma}$ **(%)**
0	45.16 ± 1.60	1.09 ± 0.02	-	-
10	42.93 ± 1.50	1.03 ± 0.02	- 4.63	- 5.63
20	41.29 ± 1.49	0.98 ± 0.01	- 7.01	- 7.42
30	39.89 ± 1.43	0.95 ± 0.01	- 11.59	- 11.99
40	39.02 ± 1.40	0.93 ± 0.01	- 12.96	- 12.59
50	38.27 ± 1.31	0.91 ± 0.01	- 18.38	- 18.20

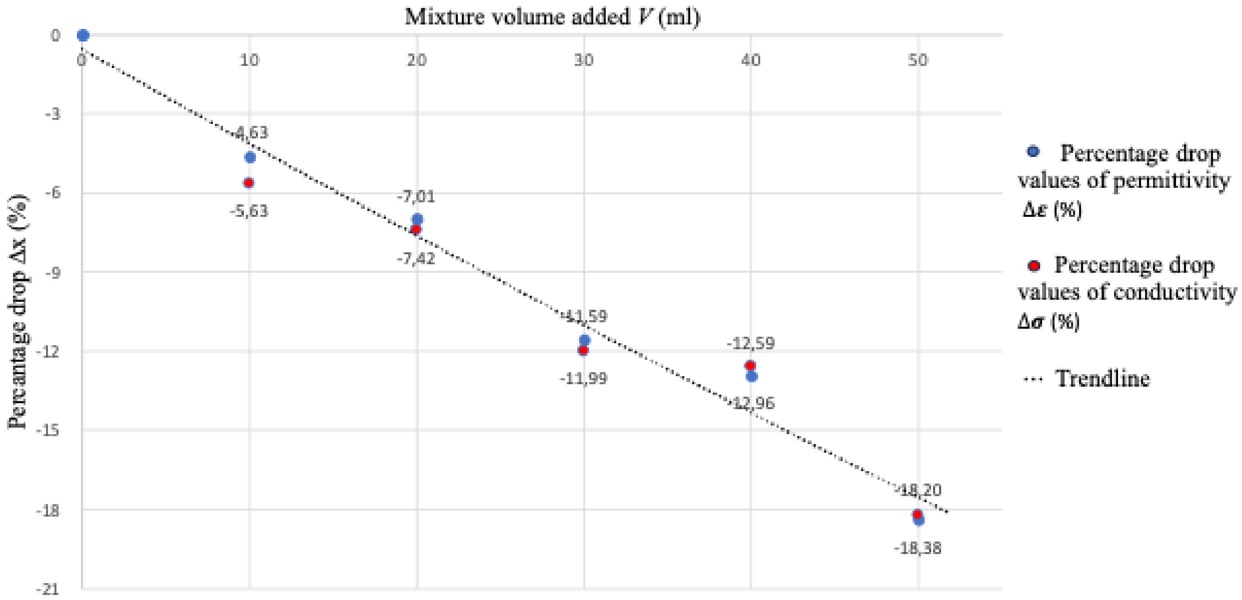

Figure 3.3: Percentage decrease in permittivity and conductivity with increasing volume of mixture added to the initial brain phantom (based on Table 3.3)

4. DISCUSSION

The main findings of this work were the development of a suitable ischemic stroke progression mixture that behaved as expected under experimental constraints. Two formulations were tested, both aiming for a controlled drop in dielectric properties of a brain phantom to mimic ischemic onset. While each had advantages, one better matched literature-based targets and volume limitations.

Mixture performance evaluation

Sample 1 (10 ml IPA, 5 ml water, 0.1 g salt) was added in 15 ml steps to 100 ml brain phantom. Although designed to achieve ~5% drops per step, the target 15% permittivity reduction was only reached after 75 ml—exceeding volume limits (syringe capacity 150 ml, with 100 ml already used by the brain). Despite smooth progression, this mixture was impractical due to its excessive requirement.

Knowing the influence of each component (IPA reduces ε and σ, water increases ε and lowers σ, salt increases σ), we adjusted the formulation. In Sample 2 (20 ml IPA, 5 ml water, 0.1 g salt), ~5% permittivity drops were achieved per 10 ml step. Within 50 ml, decreases reached 18.38% (ε) and 18.20% (σ), staying well within limits. Polynomial fits (Figures 3.2–3.3) confirmed that the 15% drop was reached at ~42 ml, allowing precise modeling of ischemic progression at chosen stages (3%, 6%, 9%, 12%, 15%).

Suitability of the improved mixture

Sample 2 clearly met the simulation goals. Its drop patterns in permittivity and conductivity were smooth, consistent, and near-linear, closely reflecting reported ischemic tissue behavior. Polynomial fits aligned well with the data, validating that IPA, water, and salt interacted as intended. This demonstrates the suitability of the liquid-based approach and supports its use in future controlled infusion experiments.

Limitations and suggestions

Some limitations remain. Manual mixing may have caused inconsistencies from salt sedimentation, affecting conductivity. The phantom was homogeneous, unlike more anatomically realistic multilayered head models (e.g., [19]). Stroke is localized and dynamic, not a uniform volume-wide change. Future improvements could include 3D-printed compartments or layered phantoms to better replicate ischemia progression.

Potential enhancement

Although Sample 2 performed well, refinements are possible. A slightly reduced IPA (~18 ml) and water (~4.5 ml) content, with constant salt, could yield slower and more linear drops, improving control. This adjustment would also leave extra volume for flexibility and compensation in real experiments. Such optimization could produce a more precise and practical progression model.

5. CONCLUSION

This project achieved its primary aim of developing a liquid brain phantom to simulate early ischemic stroke by reproducing a progressive decrease in dielectric properties, consistent with reported tissue behavior. A secondary fluid of distilled water, IPA, and salt was added to trigger the drop, with two mixtures tested. Both reduced permittivity and conductivity as expected, though the second mixture proved more efficient in volume-to-percentage-drop ratio, making it more practical under volume constraints. The outcomes followed a consistent trend, enabling prediction of different ischemic stages (e.g., 3%, 6%, 9%, 12%, 15%) using polynomial fits.

While the current model is simple and lacks anatomical layering or fixed spatial form, it provides a strong foundation for future work using inflatable balloons to simulate localized ischemic regions. This approach can be extended toward anatomically realistic phantoms to study stroke progression in a spatially distributed manner.

ACKNOWLEDGMENT

I would like to thank Ing. Tomáš Pokorný, Ph.D. for his professional guidance and valuable advice during the preparation.

REFERENCES

[1] “Stroke - What Is a Stroke? | NHLBI, NIH.” Accessed: Apr. 12, 2025. [Online]. Available: https://www.nhlbi.nih.gov/health/stroke

[2] A. Fhager, S. Candefjord, M. Elam, and M. Persson, “Microwave Diagnostics Ahead: Saving Time and the Lives of Trauma and Stroke Patients,” *IEEE Microwave Magazine*, vol. 19, no. 3, pp. 78–90, May 2018, doi: 10.1109/MMM.2018.2801646.

[3] V. L. Feigin, B. Norrving, and G. A. Mensah, “Global Burden of Stroke,” *Circulation Research*, vol. 120, no. 3, pp. 439–448, Feb. 2017, doi: 10.1161/CIRCRESAHA.116.308413.

[4] V. L. Feigin *et al.*, “World Stroke Organization: Global Stroke Fact Sheet 2025,” *Int J Stroke*, vol. 20, no. 2, pp. 132–144, Feb. 2025, doi: 10.1177/17474930241308142.

[5] CDC, “Stroke Facts,” Stroke. Accessed: Apr. 12, 2025. [Online]. Available: https://www.cdc.gov/stroke/data-research/facts-stats/index.html

[6] “Mid-point evaluation of the implementation of the WHO global action plan for the prevention and control of noncommunicable diseases 2013–2020 (NCD-GAP).” Accessed: Apr. 12, 2025. [Online]. Available: https://www.who.int/publications/m/item/mid-point-evaluation-of-the-implementation-of-the-who-global-action-plan-for-the-prevention-and-control-of-noncommunicable-diseases-2013-2020-(ncd-gap)

[7] R. L. Sacco *et al.*, “An Updated Definition of Stroke for the 21st Century: A Statement for Healthcare Professionals From the American Heart Association/American Stroke Association,” *Stroke*, vol. 44, no. 7, pp. 2064–2089, Jul. 2013, doi: 10.1161/STR.0b013e318296aeca.

[8] “Prevention And Treatment Of Ischemic Stroke - Anna’s Archive.” Accessed: Apr. 12, 2025. [Online]. Available: https://annas-archive.org/md5/7114f2aa333b365c6e38cd3c64948501

[9] “Stroke: Pathophysiology, Diagnosis, and Management (Expert Consult - Online and Print) - Mohr MS MD, J. P.; Wolf MD, Philip A.; Moskowitz MD, Michael A.; Mayberg MD, Marc R; Von Kummer MD FAHA, Rudiger: 9781416054788 - AbeBooks.” Accessed: Apr. 13, 2025. [Online]. Available: https://www.abebooks.com/9781416054788/Stroke-Pathophysiology-Diagnosis-Management-Expert-1416054782/plp

[10] S. Semenov, T. Huynh, T. Williams, B. Nicholson, and A. Vasilenko, “Dielectric properties of brain tissue at 1 GHz in acute ischemic stroke: Experimental study on swine,” *Bioelectromagnetics*, vol. 38, no. 2, pp. 158–163, 2017, doi: 10.1002/bem.22024.

[11] T. Pokorny, D. Vrba, J. Tesarik, D. B. Rodrigues, and J. Vrba, “Anatomically and Dielectrically Realistic 2.5D 5-Layer Reconfigurable Head Phantom for Testing Microwave Stroke Detection and Classification,” *International Journal of Antennas and Propagation*, vol. 2019, no. 1, p. 5459391, 2019, doi: 10.1155/2019/5459391.

[12] D. O. Rodriguez-Duarte *et al.*, “Experimental Validation of a Microwave System for Brain Stroke 3-D Imaging,” *Diagnostics*, vol. 11, no. 7, Art. no. 7, Jul. 2021, doi: 10.3390/diagnostics11071232.

[13] “EMVision | Portable Brain Scanner | Stroke Diagnosis and Monitoring.” Accessed: Apr. 13, 2025. [Online]. Available: https://emvision.com.au/

[14] “Homepage -,” EMTensor. Accessed: Apr. 13, 2025. [Online]. Available: https://www.emtensor.com/

[15] “Introducing Strokefinder: Microwave Helmet That Identifies Stroke Type: NY Neurology Associates: Neurologists.” Accessed: Apr. 13, 2025. [Online]. Available: https://www.nyneurologists.com/blog/introducing-strokefinder-microwave-helmet-

that-identifies-stroke-type
[16] B. McDermott *et al.*, “ANATOMICALLY AND DIELECTRICALLY REALISTIC MICROWAVE HEAD PHANTOM WITH CIRCULATION AND RECONFIGURABLE LESIONS,” *PIER B*, vol. 78, pp. 47–60, 2017, doi: 10.2528/PIERB17071805.
[17] J. Liu, L. Chen, H. Xiong, and Y. Han, “Review of microwave imaging algorithms for stroke detection,” *Med Biol Eng Comput*, vol. 61, no. 10, pp. 2497–2510, Oct. 2023, doi: 10.1007/s11517-023-02848-5.
[18] T. Pokorny, T. Drizdal, M. Novak, and J. Vrba, “Automated, Reproducible, and Reconfigurable Human Head Phantom for Experimental Testing of Microwave Systems for Stroke Classification,” *International Journal of Imaging Systems and Technology*, vol. 34, no. 6, p. e23200, 2024, doi: 10.1002/ima.23200.

NUMERICAL STUDY OF THE EFFECT OF NUMBER OF ANTENNAS AND BANDWIDTH ON IMAGING OF FOREIGN OBJECTS IN THE HUMAN BODY

Author: Bc. Adam Fojtík
Supervisor: doc. Ing. Ondřej Fišer, Ph.D.
Consultant: Ing. Jakub Kollár

ABSTRACT

This project specifically deals with a numerical study of the influence of the number of antennas and bandwidth on the imaging of foreign objects in the human body. This practically means that it is a matter of determining the most optimal number and bandwidth of antennas. These are UWB antennas designed by the Bio-electromagnetism team of the Faculty of Biomedical Engineering of the Czech Technical University in Prague, for microwave imaging. [1] Delay and Sum is considered as a reconstruction algorithm. Pulmonary embolism and a metal projectile were chosen as the displayed objects in this project. Pulmonary embolism is currently the third most common acute cardiovascular disease globally. A metal projectile was chosen as the second displayed object. The choice of this object was inspired by the military conflicts constantly taking place all over the planet. [2] [3] From the results of that annual project, the UWB antenna system and 2D DAS reconstruction algorithm seem functional.

1. INTRODUCTION

Conventional and tomographic examinations using ionizing radiation are currently the standard available to every patient. However, this method of examination has several disadvantages. The main and most significant disadvantage is the very use of ionizing radiation, which is more harmful to the human body. One of the possible and at the same time safe alternatives to ionizing radiation is microwave radiation. And it is precisely this kind of ripple that this project deals with.

2. METHODS

2.1 Numerical study in the Sim4Life

Numerical simulation is divided into three main parts, which are Model, Simulation and Analysis. In the Model section, 3D objects are created according to user requirements. This project involves a heterogeneous model of the human body, UWB antenna, Matching media (medium between UWB antenna and heterogeneous model) and a foreign object. Since the project only deals with 2D imaging, it was important to choose a suitable imaging space around which the antennas will be deployed. This space is shown in Figure 2.1. As for the foreign objects, they were imported in the case of the 9 × 19 mm Luger ammunition and modeled manually in the case of the PE. Both objects were placed in the observed area. It should be noted that the observed area was chosen regarding the most frequent location of foreign objects.

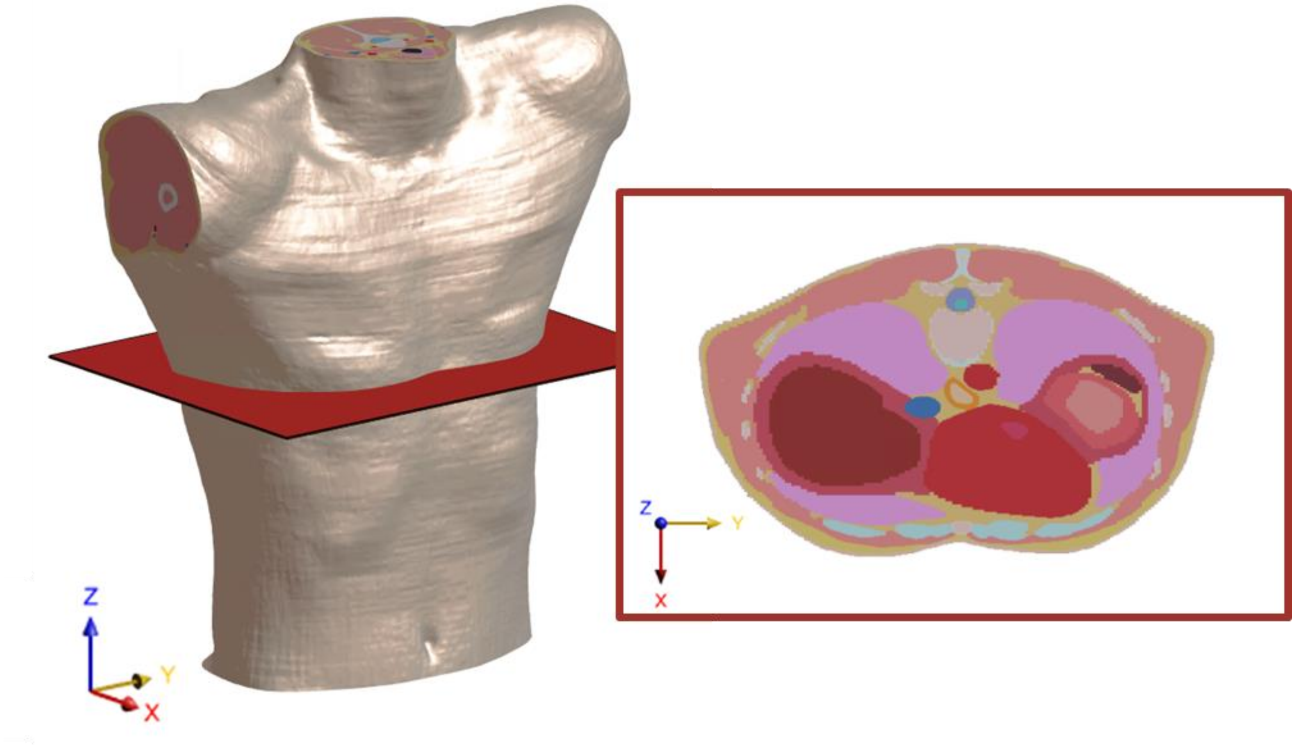

Figure 2.1: Image of the selected observed area

When the distribution of UWB antennas around the observation area is shown in Figure 2.2. These UWB antennas were then switched on gradually so that the optimal number of UWB antennas around the observed area could be found and the best possible resolution could be achieved.

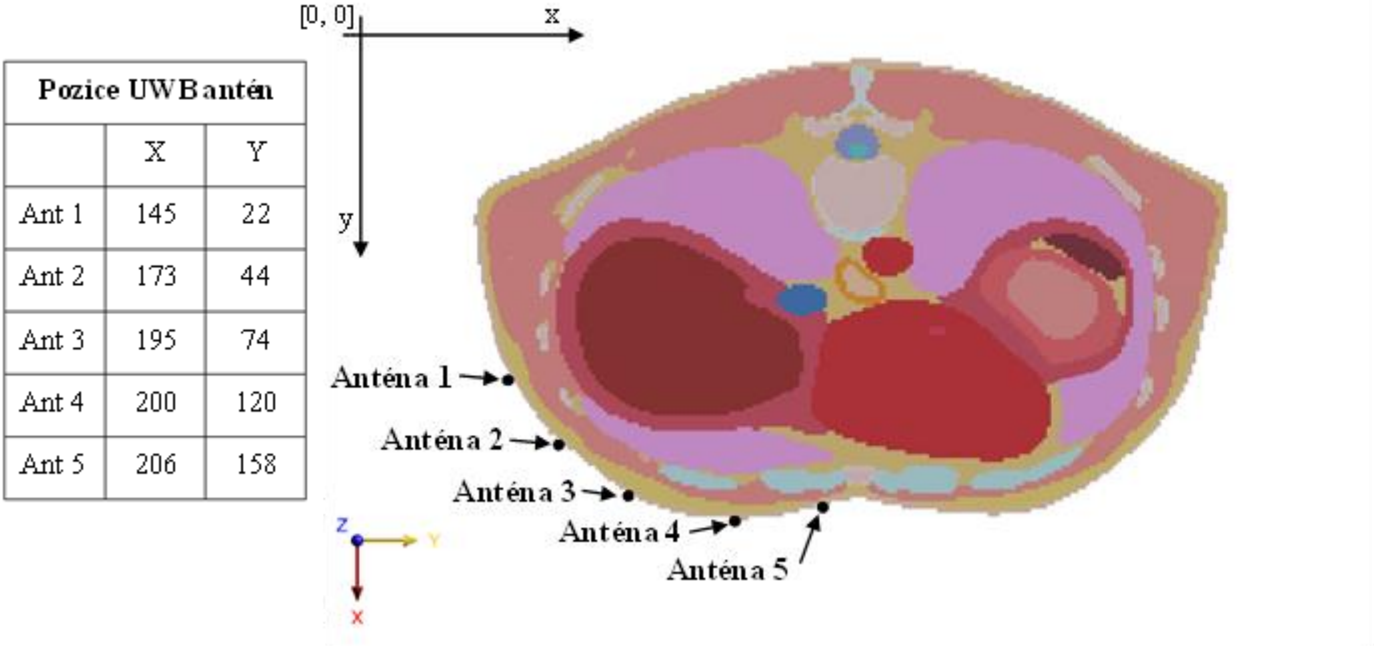

Pozice UWB antén		
	X	Y
Ant 1	145	22
Ant 2	173	44
Ant 3	195	74
Ant 4	200	120
Ant 5	206	158

Figure 2.2: Position (pozice) of UWB antennas (antén/a) around the observation area

In the Simulation section, the material properties of the objects (dielectric parameters) are set, as well as the choice of the type of simulation or the method of excitation of UWB antennas. The UWB antenna was excited by a Gaussian type of pulse and since this project also dealt with the effect of bandwidth, these frequencies were two. The first was 3.5 GHz and the second 5 GHz, when both frequencies corresponded to the central frequency of the given frequency band (fC). The waveforms of the exciting Gaussian pulses in the frequency domain. Such a Gaussian pulse can then be characterized by parameters such as bandwidth (BW), central frequency (fC), fD and fH. [4]

2.2 Delay and Sum algorithm in the MATLAB

In this chapter, a small space will be devoted to detailing the individual steps that lead to the resulting image reconstruction of the location of the foreign object. The first step is to import calculated results from numerical simulations in csv data format into the MATLAB environment. The following steps occurred here. The first was to subtract the signal from the simulation with the foreign object from the signal from the simulation without the foreign object. After this subtraction, there was a localized difference, under which in this case we can imagine a foreign object. Further signal modification consists in deducing the time when the signal passes through the UWB antenna and further dividing the thus modified signal by two. This step is necessary because the sent signal travels to the foreign object and back again, so the reconstruction algorithm would show us the foreign object at twice the distance than it is. The next step was the creation of a distance matrix where the zero distance was placed in the position of the active UWB antenna and the rest of the values in the matrix were calculated according to the distance to the active UWB antenna. The next step was to create a time matrix. This time matrix was calculated using the matrix distances and knowledge of the speed of propagation of EM waves in biological tissue. After calculating the time matrix for all active UWB antennas, an amplitude matrix could be created. This was created by recording voltage values as a function of time. These times were compared to the time matrix. Finally, by combining these amplitude matrices of all active UWB antennas, an amplitude matrix showing the location of the foreign object was created.

3. RESULTS

Numerical simulation results were obtained for individual foreign objects, given frequency bands and for different numbers of active UWB antennas. PE and ammunition positions were constant in this project. What was different here was the number of active UWB antennas. Switching on individual UWB antennas took place after two, three, four and finally all five UWB antennas. Due to the limitation of the scope of this contribution, only one of the resulting reconstructions will be shown here, namely for PE, two active UWB antennas and for the frequency 1– 6 GHz (shown in Figure 3.1).

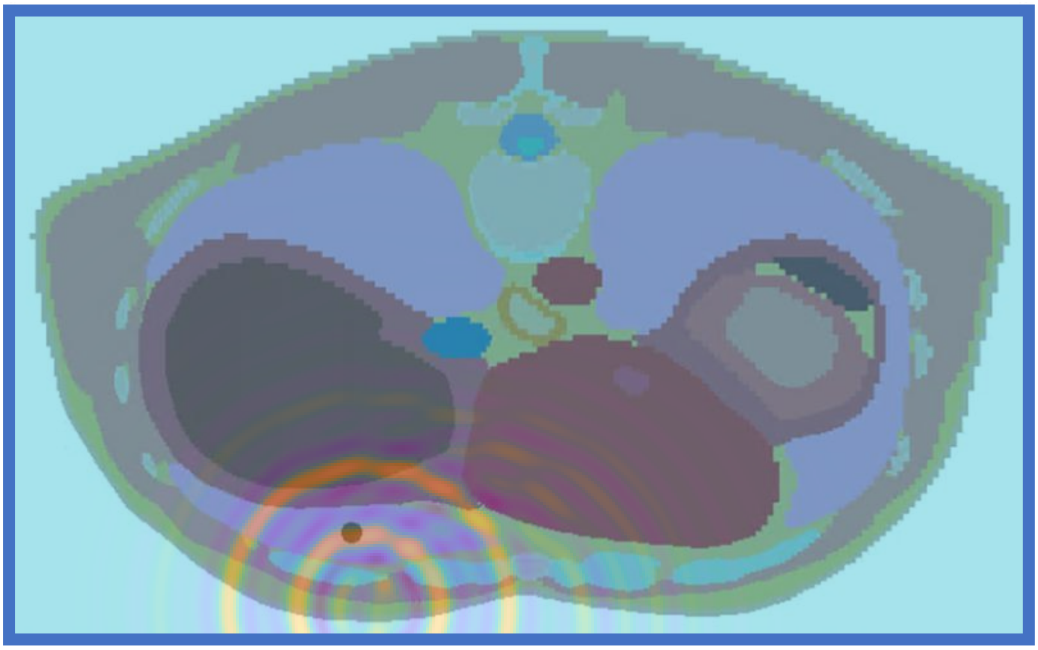

Figure 3.1: Image reconstruction with two active UWB antennas during PE imaging in the frequency band 1− 6 GHz

4. DISCUSSION

Although the system shows slight inaccuracies in some cases, it is still able to estimate the position of a foreign object relatively accurately. While the system appears to be very reliable and accurate for the 1− 6 GHz frequency band for PE imaging through two active UWB antennas. Furthermore, it should be mentioned that the inaccuracies of the reconstructions are most likely due to the imperfection of the DAS reconstruction algorithm part, where one constant speed was always used to calculate the time matrix through the matrix distances and the propagation speed of EM waves through biological tissue, namely the speed of EM in muscle tissue. Although this speed does not change dramatically regarding the type of biological tissue, this could have been the reason for the difference in determining the position of the foreign object in some cases of up to 2 cm. It should also be mentioned that there were bones and cartilaginous tissue in the path of the EM waves, which will reflect part of the waves, thus complicating the reconstruction itself.

5. CONCLUSION

Based on the results of that annual project, the UWB antenna system and the 2D DAS reconstruction algorithm can be considered functional. However, in the future it would be advisable to consider, for example, 3D DAS reconstruction, possibly another variant of the DAS algorithms and the distribution of UWB antennas around the entire heterogeneous model of the human body for better localization of foreign objects in various ways throughout the entire imaged area.

6. ACKNOWLEDGMENT

I would like to thank the supervisor of the thesis doc. Ing. Ondřej Fišer, Ph.D. for his valuable advice and professional management of the project. I would also like to thank my consultant Ing. Jakub Kollár for his efforts, activity and valuable advice during the creation of this project.

REFERENCES

[1] O. Fišer, V. Hrubý, J. Vrba, T. Dřížďal, J. Tesařík, and J. V. Jr, "UWB Bowtie Antenna for Medical Microwave Imaging Applications," 2022. [Online]. Available: https://ieeexplore.ieee.org/document/9743695/figures#figures. [Access will take place on 15.06.2025].

[2] Czech Society of Cardiology, "Pulmonary Embolism," 2025. [Online]. Available: https://www.kardio-cz.cz/plicni-embolie.html. [Accessed 06/20/2025].

[3] R. DiCarlo, "Secretary-General's remarks to the Security Council - on Ukraine," 2024. [Online]. Available: https://www.un.org/sg/en/content/sg/statement/2024-11-18/secretary-generals-remarks-the-security-council-ukraine. [Accessed 06/20/2025].

[4] B. J. Kollár, "3D UWB radar system for monitoring radiofrequency ablation of liver tumors," 2024. [Online]. Available: https://dspace.cvut.cz/. [Accessed 06/18/2025].

Design of a supercascode switching device for a multiphase electroporation system for use in irreversible electroporation in vitro

O. Z. Bílý

Department of Biomedical Technology, Faculty of Biomedical Engineering,
Czech Technical University in Prague, Kladno, Czech Republic

INTRODUCTION

The most common heart rhythm disorder in the world is atrial fibrillation. It is very serious rhythm disorder, which could result in a stroke in the case of complications. This disorder is usually treated with use of medication or by surgery. In the case of surgery, the main problem in the treatment lies in the thermal effect created during catheterization procedures. The result of this thermal effect is irreversible damage to the surrounding tissue, which can cause serious health problems such as permanent paralysis of the diaphragm.

The thermal effect during catheterization procedures is limited by the irreversible electroporation technique, using ultra-short high-voltage pulses. The advantage of this method is the minimization of the time for which the tissue will be heated. During electroporation, the cells are exposed to high-voltage electrical impulses, and the permeability of their membrane increases temporarily [1]. By applying high-voltage square pulses, an electric field is created, which results in the temporary depolarization of the cell membrane and the formation of hydrophilic pores that allow the entry of macromolecules from the extracellular environment or lead to the death of the given cell [2].

In clinical practice this method is called pulsed field ablation (PFA) and is gradually replacing the conventional ablation methods used so far (for example, radiofrequency ablation or cryoablation) and is becoming a routine procedure for the treatment of cardiac arrhythmias. However, it is still a relatively new method whose processes need to be thoroughly researched. Therefore, there is an increased need for *in vitro* experiments that would help to clarify the unexplored mechanisms of electroporation. However, there are currently not many commercially available devices on the market that would allow for the performance of complex experiments with a wide range of sequences. [3-5]

The aim of this work is to design and implement high-voltage switching elements for a laboratory generator of high-voltage multiphasic pulses for the study of electroporation on adherent cell cultures. These switching elements using supercascode topology will be capable of switching voltages up to 3 kV and currents up to 5 A. Also, the design of these switches will follow the ČSN EN 61010-1 standard [6], which specifies safety requirements for electrical measurements, control and laboratory equipment.

METHODS

A high-voltage switch was developed using a supercascode topology, a combination of several series-connected JFETs with a single low-voltage MOSFET. The MOSFET served as the control element, triggering the cascade by modulating the drain–source voltage across the JFETs. Protective resistors, zener diodes, and balancing capacitors were added to stabilise voltage distribution and prevent breakdown. The final design of the switch ensured reliable switching of up to 3 kV. Its performance was verified with simulation in software Microcap, where a 15 V gate signal controlled the MOSFET.

Following the simulation results, the switch was implemented on a printed circuit board designed in Autodesk Fusion 360. The board was separated into low- and high-voltage domains, with galvanic isolation provided by a gate driver and DC/DC converter. Particular attention was paid to creepage and clearance distances in accordance with ČSN EN 61010-1 safety requirements. For 3 kV DC operation under pollution degree 1, minimum clearances of 5.76 mm and creepage distances of 11.79 mm were required [6].

Four switches were created and evaluated. Characterisation focused on rise and fall times, leakage current, and switching losses. During evaluation, a half-bridge arrangement of two switches was used, with outputs taken from the midpoint. Control signals were supplied by an Arduino Mega 2560, while a modified electroporation device [7] provided the high-voltage input. Oscilloscope measurements determined switching delays and waveform fidelity, while energy losses were estimated by monitoring voltage drops across a capacitor bank during repeated switching cycles. More specifically, the equation used for calculating the losses E_z (J) is given in formula (1):

$$E_z = \frac{\frac{1}{2}\cdot C\cdot\left(U_1{}^2 - U_2{}^2\right)}{n}, \tag{1}$$

where $C = 50$ µF, which is the capacitance of the capacitor bank, U_1 (V) is the original voltage value, U_2 (V) indicates the voltage value to which the original value has dropped, and n (-) is the total number of switching operations.

To assess potential usage for electroporation, an experiment was designed using HL-1 cardiac muscle cells cultured in 96-well plates. During this experiment, cells are exposed to biphasic square pulses (2 µs duration, 5 µs interval, 216 pulses per burst, 20 bursts at 1 Hz). To achieve different electric fields switching voltage is adjusted in accordance with simulation data. Following exposure, cells are to be stained with propidium iodide and Hoechst dye to evaluate membrane integrity and nuclear morphology. With fluorescence microscopy it is possible to distinguish viable from non-viable cells, enabling quantification of electroporation-induced death rates.

RESULTS

The supercascode switching element was successfully designed, simulated, and fabricated (final version shown in Figure 1). Four prototype boards were assembled and tested. In both simulation and experimental measurements, the switches operated reliably up to several hundred volts, with extrapolated design parameters allowing for 3 kV operation.

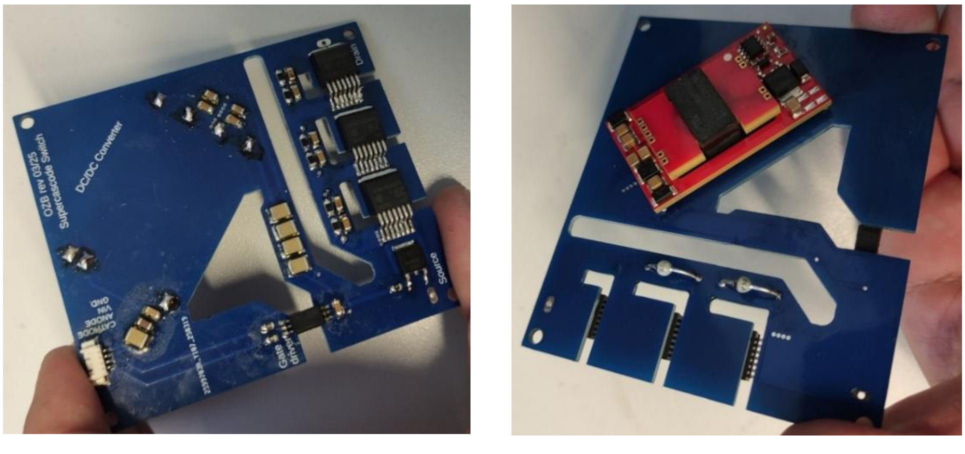

Figure 1. Final version of the switch after modifications

Oscilloscope measurements revealed a switching delay of approximately 200 ns relative to the control signal. The rise and fall times were 148 ns and 130 ns, respectively, confirming fast switching behaviour. Minor oscillations observed at the signal edges were attributed to parasitic capacitances and inductances, as the switches were tested under no-load conditions without additional damping.

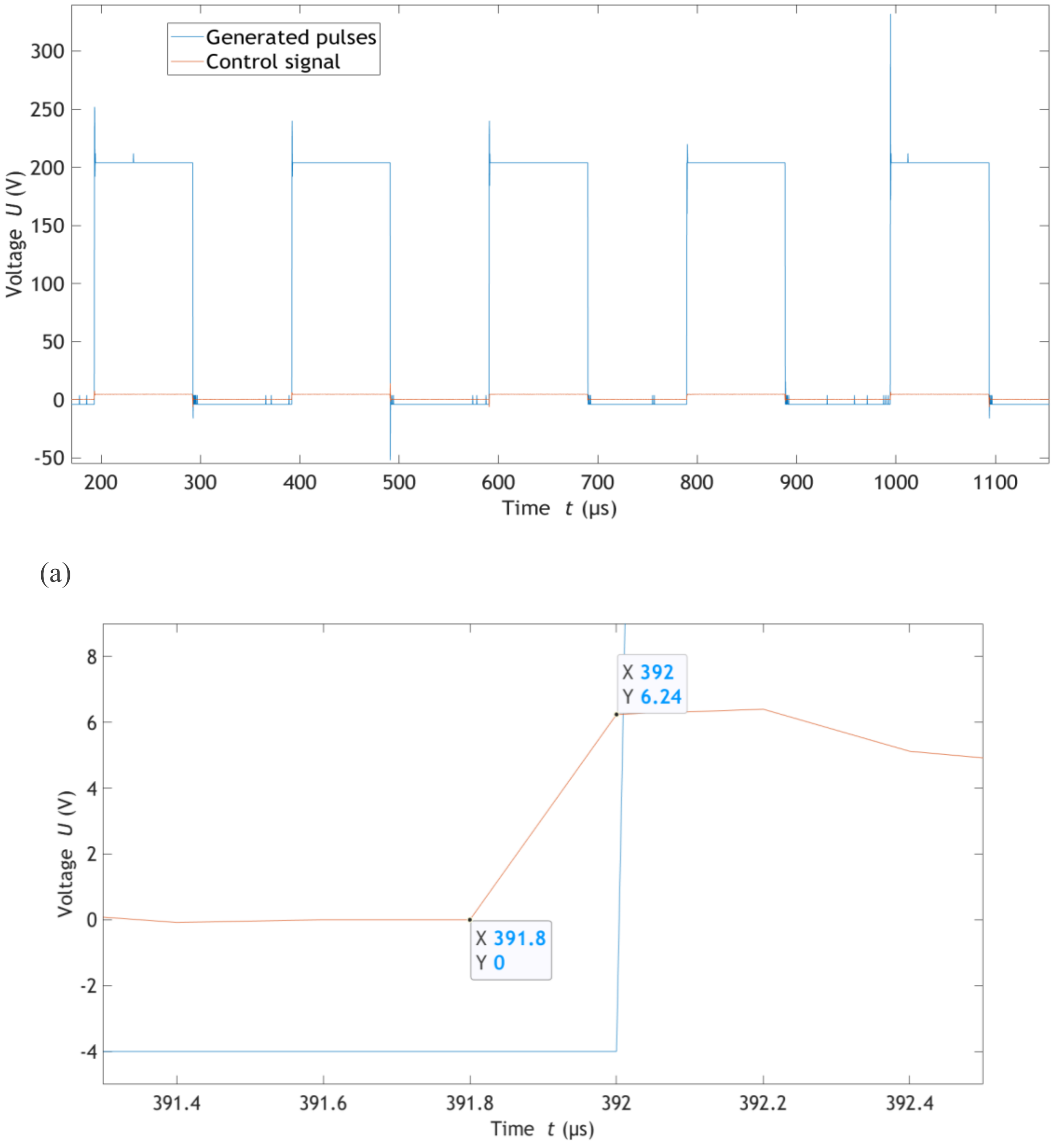

(a)

(b)

Figure 2. The generated 100 μs pulses with the control signal (a) and a detail of the switching delay compared to the control signal (b)

Switching losses were estimated using a 50 μF capacitor bank. Based on voltage drop analysis over repeated switching cycles of 1 μs pulses (shown in Figure 3), total losses were calculated at approximately 4.4 mJ with equation in formula (1). Leakage current in the off state was determined from impedance measurements. For an operating voltage of 3 kV, the residual current was estimated at 1.42 mA.

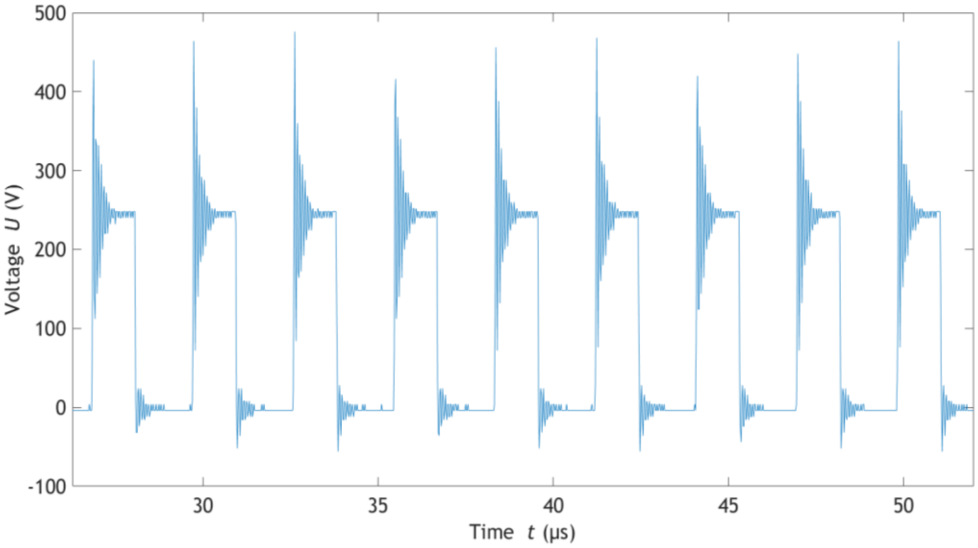

Figure 3. The generated 1 µs pulses used to determine losses

During prototype assembly, a design error in the DC/DC converter footprint required manual modification, which delayed biological validation. Consequently, the planned electroporation experiment is yet to be carried out. Nonetheless, the electrical performance of the switches demonstrates their suitability for integration into a high-voltage, multiphasic electroporation system.

DISCUSSION

A total of 4 functional switching elements capable of switching high voltages with minimal losses and delays were developed for inducing electroporation as part of research into the electroporation phenomenon using monophasic and multiphasic square wave signals. The developed switching elements are rated for voltages up to 3 kV. During testing, it was exposed to up to 500 V, whereas it was able to deliver 1 µs and 100 µs long pulses with a minimum delay of approximately 200 ns in comparison to the control signal. The rise time of the square wave had a length of 148 ns and a fall time of 130 ns, the residual current of the switch in the open state at a voltage of 3 kV is 1.42 mA. Furthermore, the losses when switching the switching element were calculated to be 4.44 mJ.

The visible ripple at the ends of the leading edges was primarily caused by the absence of load during testing and by inappropriate shielding of the conductors. Also, during the development, problems occurred with the soldering pads for the DC-DC converter. More specifically, while creating the layout of the PCB, the pads were mirror-imaged compared to the recommended layout. This problem caused a delay of the entire project, therefore the verification experiment, demonstration of the possibility of using these switches for inducing cell death by irreversible electroporation *in vitro*, is yet to be carried out. At the same time, the devices used, and especially the high voltage source, were not an ideal choice for testing the properties of the switching element.

Nevertheless, thanks to the modification of this device, all the necessary parameters were measured. Given the satisfactory results of the simulation and testing, it could be assumed that switches are able to generate a pulsed electric field for successful cell killing by electroporation. In the future, it is planned to perform the verification experiment and continue with the development of other components for the multiphasic electroporator, which will find use as a laboratory device designed for research into the electroporation phenomenon.

CONCLUSION

In total, four switching elements with supercascode topology capable of switching high voltages up to 3 kV with minimal losses and delays were designed and subsequently implemented. Due to poor design of the DC-DC converter location, the project was significantly delayed, therefore switches were not yet tested for possible use in laboratory practice for research into the electroporation phenomenon. In the future, it is planned to use these switches as components for a multiphase electroporator, which will be the main output of the subsequent master thesis.

ACKNOWLEDGMENT

In vitro experiments will be performed at the 3rd Faculty of Medicine, Charles University. Using a switch sample, demonstrate the possibility of using it in *in vitro* electroporation to induce cell death in adherent cell cultures (e.g., HL-1 line), where, using commercially available electrodes on a 96-well system, determine the threshold for induction of cell death by electroporation depending on the electric field using H-FIRE or similar biphasic pulses.

REFERENCES

[1] NAPOTNIK, Tina Batista, Tamara POLAJŽER a Damijan MIKLAVČIČ. *Cell death due to electroporation – A review* [online]. 141. 2021. ISSN 1567-5394.

[2] Hyder, I., Eghbalsaied, S. a Kues, W.A. *Systematic optimization of square-wave electroporation conditions for bovine primary fibroblasts* [online]. *BMC Mol and Cell Biol* **21**, 9 (2020).

[3] Reddy VY, Dukkipati SR, Neuzil P, Anic A, Petru J, Funasako M, Cochet H, Minami K, Breskovic T, Sikiric I, Sediva L, Chovanec M, Koruth J, Jais P. *Pulsed Field Ablation of Paroxysmal Atrial Fibrillation: 1-Year Outcomes of IMPULSE, PEFCAT, and PEFCAT II.* JACC Clin Electrophysiol. 2021 May;7(5):614-627. doi: 10.1016/j.jacep.2021.02.014. Epub 2021 Apr 28. PMID: 33933412.

[4] Reddy VY, Anter E, Peichl P, Rackauskas G, Petru J, Funasako M, Koruth JS, Marinskis G, Turagam M, Aidietis A, Kautzner J, Natale A, Neuzil P. *First-in-human clinical series of a novel conformable large-lattice pulsed field ablation catheter for pulmonary vein isolation.* Europace. 2024 Mar 30;26(4): euae090. doi: 10.1093/europace/euae090. PMID: 38584468; PMCID: PMC11057205.

[5] Maccioni S, Sharma R, Lee DD, Haltner A, Khanna R, Vijgen J. *Comparative Safety of Pulsed Field Ablation and Cryoballoon Ablation Technologies for Pulmonary Vein Isolation in Patients with Paroxysmal Atrial Fibrillation: A Critical Literature Review and Indirect Treatment Comparison*. Adv Ther. 2024 Mar;41(3):932-944. doi: 10.1007/s12325-023-02765-x. Epub 2024 Jan 8. PMID: 38185778; PMCID: PMC10879347.

[6] ČSN EN 61010-1 ed.2, "*Safety requirements for electrical equipment for measurement, control, and laboratory use – Part 1: General requirements*," Prague, Czech Republic: Czech standardization agency, 2011.

[7] BÍLÝ, Ondřej Zdeněk. *Elektroporační systém pro elektroporaci adherentních buněčných kultur a studium hemolýzy při elektroporační terapii srdečních arytmií*. Bachelor Thesis. Kladno: Czech technical university in Prague, Faculty of biomedical engineering, 2024.

Modelling and experimental analysis of cell electrotransfection for biomedical applications

A. Danilkova[1]

[1]Faculty of Biomedical Engineering, CTU in Prague, Czech Republic

Abstract — Electrotransfection is a non-viral method of gene transfer that uses electrical pulses to temporarily increase the permeability of the cell membrane. This technology enables the entry of DNA, RNA or proteins into cells and is used in gene therapy, tissue engineering and the treatment of cardiovascular diseases. This study combines numerical simulations and experimental analysis to determine the optimal electric field value for achieving a high transfection efficiency while maintaining cell viability. The results show that the highest transfection efficiency was obtained at 1200 V/cm, with low cell mortality. Higher field intensities further increased the number of transfected cells but were accompanied by a marked rise in cell death. These results provide practical guidance for optimizing electrotransfection protocols in cardiovascular research.

1. INTRODUCTION

Electrotransfection (ET) is a non-viral method used to increase the uptake of exogenous macromolecules, such as nucleic acids or proteins, into cells. The underlying mechanism is electroporation, in which pulsed electric fields transiently increase cell membrane permeability[1,2]. However, excessive permeabilization may lead to irreversible membrane damage and cell death[3].

The efficiency of ET depends on several parameters, including pulse intensity, duration, number and shape of pulses, cell type, and medium composition. Due to the complexity of these factors, there is no universal protocol and settings must always be optimized for each application[4–7]. Numerical modelling and simulations play a crucial role in this area as they predict the distribution of the electric field and help reduce the cost and duration of experimental optimization[8–10].

Electrotransfection demonstrates significant therapeutic potential in arrhythmogenic cardiomyopathy (ACM). This genetically determined myocardial disease leads to cardiac arrhythmias and gradual degeneration and replacement of muscle tissue with connective tissue. Currently, therapy is aimed only at relieving symptoms (pharmacotherapy, catheter ablation, and implantable cardioverter defibrillators (ICDs)), and there is no causal treatment. Gene electrotransfer (GET) may thus become an alternative therapeutic approach that will allow targeted modulation of gene expression or even regeneration of cardiac tissue[11–15].

The aim of this work was to determine the optimal electric field intensity for maximum transfection efficiency while preserving cell viability, thereby contributing to the potential future application of ET in cardiology, particularly for arrhythmogenic diseases.

2. METHODS

Numerical simulations were performed in COMSOL Multiphysics using the Electric Currents module. A three-dimensional model of a microtiter well was constructed, comprising the cell layer, culture medium, surrounding air, and gold electrodes. The geometry included the applied voltage, electrode dimensions, and inter-electrode distances as variable parameters (Figure 1).

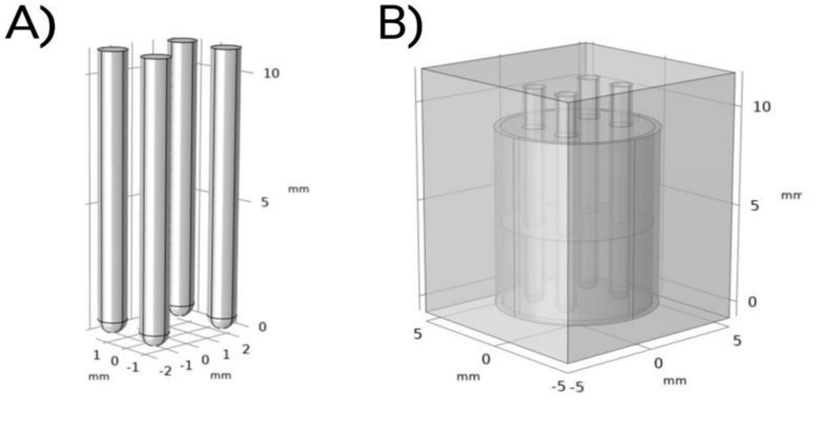

Figure 1. Geometry of a microtiter well model. (A) Model of electrodes. (B) Final geometric model.

To approximate real experimental conditions, appropriate physical properties—electrical conductivity and relative permittivity—were assigned to each component of the model.

Table 1. Relative permittivity and electrical conductivity values of materials used.

Material	**Electrical conductivity σ (S/m)**	**Relative permittivity ε (-)**
Water	0.56	1
Air	1×10^{-9}	1
Acrylic plastic	1×10^{-5}	1
Gold	$\Sigma_{solid}(T)$	1

Simulations were performed at four different voltages (380 V, 450 V, 530 V and 650 V). The simulation results were exported to MATLAB, where the electric field intensity values in the cell layer plane were interpolated.

For the experimental part, in vitro electrotransfection of cells was performed at intensities of 1000, 1200 and 1400 V/cm, applying different electroporation protocols (2×20 ms, 4×10 ms, 8×5 ms, 20×1 ms and 40×1 ms). Cells were classified based on their fluorescence colour: blue indicated untransfected cells, red indicated dead cells and green indicated transfected cells.

Cell detection was performed using image processing in MATLAB, where the centroids were identified and assigned the corresponding electric field intensity values. The statistical analysis included determining the intensity modes at which transfection occurred most frequently and comparing the effectiveness of individual protocols.

3. RESULTS

For each voltage value, graphs of the electric field distribution in the cell layer were created. The maximum and average values of electric field intensity were calculated in COMSOL Multiphysics and are summarised in Table 2.

Table 2. Average and maximum electric field intensity values at different applied voltages.

Applied voltage V_0 (V)	**Maximum field intensity (V/cm)**	**Average field intensity (V/cm)**
380	2770	814
450	3290	964
530	3870	1135
650	4750	1392

Figure 2 presents an example of cell detection at 1000 V/cm (190 cells in total), where transfected, dead, and untransfected cells were classified based on fluorescence signal. The corresponding simulated electric field distribution at 1000 V/cm is shown in Figure 3.

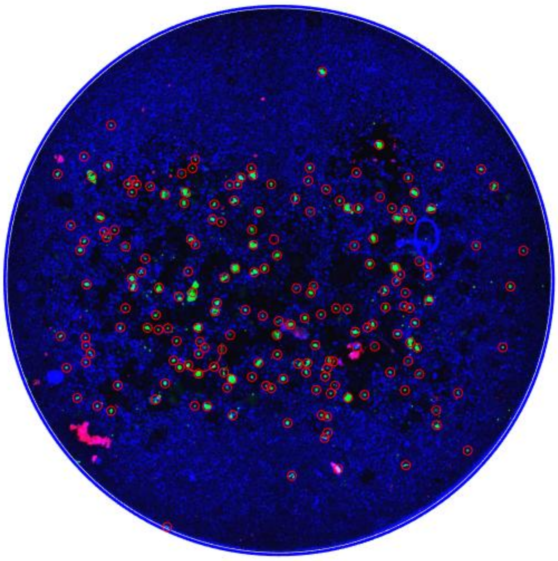

Figure 2. Transfected cells detected at 1000 V/cm. Number of cells: 190.

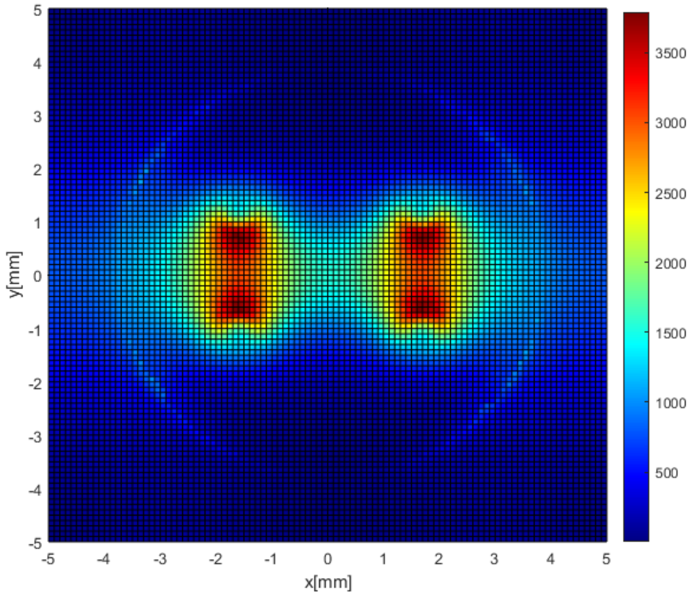

Figure 3. Simulated electric field distribution at 1000 V/cm.

The overall results for all analysed field values are summarised in Table 3, focusing on the relationship between field intensity, transfected cells, and the most frequent intensity values.

Table 3. Summary of detected cells and field characteristics.

Simulated voltage V_0 (V)	Experimental field intensity (V/cm)	Max intensity from simulations (V/cm)	Average intensity from simulations (V/cm)	Transfected cells (n)	Mode field intensity (V/cm)
450	1000	3290	964	190	800
530	1200	3870	1135	204	1600
650	1400	4750	1392	204	1500

Table 4. Dependence of transfection efficiency and cell survival on electric field intensity.

Field intensity (V/cm)	Transfected cells (%)	Dead cells (%)
1000	2,88	3,16
1200	3,16	3,03
1400	3,72	14,71

Results of different pulse protocols at 1200 V/cm are shown in Figure 4 and Table 5.

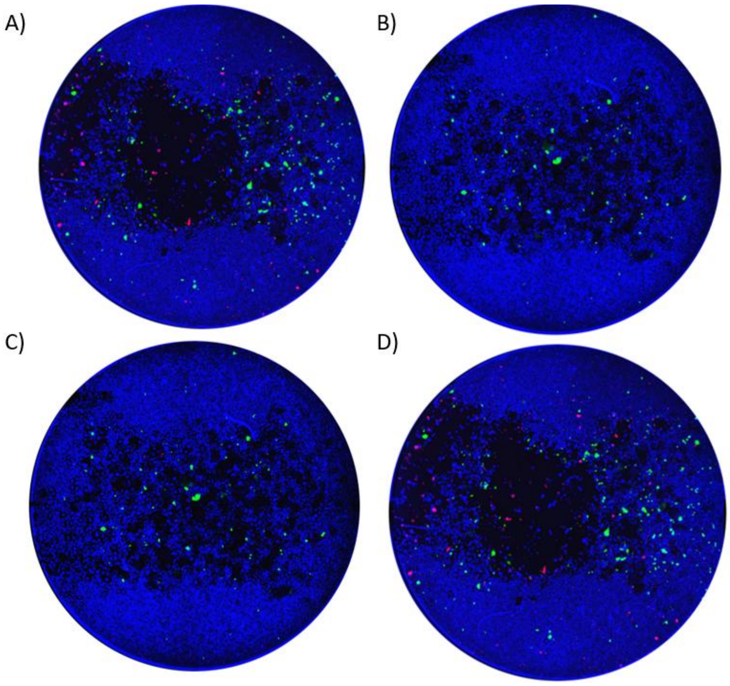

Figure 4. Microscopic images of electroporation results for different protocol settings. Green = transfected cells, red = dead cells: A) 4×10 ms; B) 8×5 ms; C) 20×1 ms; D) 40×1 ms.

Table 5. Summary of results for different protocols (at 1200 V/cm).

Protocol	Transfected cells (n)	Mode field intensity (V/cm)	Transfected cells (%)	Dead cells (%)
2×20 ms	204	1600	3,16	3,03
4×10 ms	178	1900	1,42	0,45
8×5 ms	82	2200	1,52	0,92
20×1 ms	67	800	2,75	1,21
40×1 ms	175	1900	3,03	6,83

4. DISCUSSION

The results show that electric field intensity is a key factor in electrotransfection efficiency. The highest numbers of transfected cells were observed at 1200 and 1400 V/cm, but higher intensity led to a dramatic rise in mortality (14.7%), making it unsuitable for clinical use. The optimal compromise was achieved at 1200 V/cm, where mortality did not exceed 3% while efficiency remained high.

Numerical simulations revealed significant inhomogeneity in field distribution, with maxima near the electrodes and lower intensity in the well centre. This was reflected in experiments – higher intensity regions showed more transfection, but also higher mortality. Discrepancies between COMSOL simulations and MATLAB interpolation highlight the limitations of the processing methods used. Direct data export from COMSOL could improve accuracy by preserving extreme values that interpolation smooths out.

Experiments further confirmed that pulse number and duration significantly influence transfection and viability. The 2×20 ms protocol was the most effective, while many short pulses increased mortality. This demonstrates that optimisation of electroporation parameters depends not only on field intensity but also on temporal pulse characteristics.

5. CONCLUSION

This work focused on analyzing the efficiency of cell electrotransfection using numerical simulations and in vitro experiments. The optimal electric field intensity for the protocol used (2×20 ms) was 1200 V/cm, representing the best compromise between high transfection rate and low cell mortality.

Numerical simulations showed a non-homogeneous distribution of the electric field, which was reflected in the experimental results. Although some differences between simulations and experiments were observed, the combination of both approaches proved to be crucial for the design of effective and safe protocols.

The results provide a solid foundation for further research, particularly for refining numerical models, optimizing interpolation methods, and developing prediction tools that could significantly contribute to the use of electrotransfection in biomedical applications, such as gene therapy for arrhythmogenic cardiomyopathies.

ACKNOWLEDGMENT

I would like to thank my supervisor, Assoc. Prof. Ing. Ondrej Fiser., Ph.D., for his valuable guidance, advice, and support throughout this work.

REFERENCES

[1] L.D. Cervia et al. “Current progress in electrotransfection as a nonviral method for gene delivery.” *Molecular Pharmaceutics* [online], 2018. https://doi.org/10.1021/acs.molpharmaceut.8b00207

[2] K. Steward. “An Introduction to Electroporation: A Tool for Transfection and Competent Cell Generation.” *Technology Networks*: *Cell Science* [online], 2022. Dostupné z: An Introduction to Electroporation – A Tool for Transfection and Competent Cell Generation | Technology Networks.

[3] Eagle harbor technologies. “*Electroporation*.”, [online].

Dostupné z: https://www.eagleharbortech.com/applications/electroporation/

[4] Cervia LD, Yuan F. Current Progress in Electrotransfection as a Nonviral Method for Gene Delivery. Mol Pharm. 2018 Sep 4;15(9):3617-3624. doi: 10.1021/acs.molpharmaceut.8b00207. Epub 2018 Jun 20. PMID: 29889538; PMCID: PMC6123289

[5] KANDUŠER, Maša a Mojca PAVLIN**.** Gene Electrotransfer: From Understanding the Mechanisms to Optimization of Parameters in Tissues. In: IGLIČ, Aleš, ed. *Advances in Planar Lipid Bilayers and Liposomes*. Academic Press, 2012, vol. 15, s. 77–104. ISSN 1554-4516. ISBN 9780123965332. Dostupné z: https://doi.org/10.1016/B978-0-12-396533-2.00001-X

[6] Potočnik T, Maček Lebar A, Kos Š, et al. Effect of Experimental Electrical and Biological Parameters on Gene Transfer by Electroporation: A Systematic Review and Meta-Analysis. *Pharmaceutics*. 2022;14:2700

[7] Urbanskas, E., Jakštys, B., Venckus, J., Malakauskaitė, P., Šatkauskienė, I., Morkvėnaitė-Vilkončienė, I., & Šatkauskas, S. (2024). Interplay between electric field strength and number of short-duration pulses for efficient gene electrotransfer. *Pharmaceuticals(Basel,Switzerland), 17*(7), 825. Dostupné z: https://doi.org/10.3390/ph17070825

[8] Mi Y, Xu J, Tang X, Yao C, Li C. Electroporation simulation of a multicellular system exposed to high-frequency 500 ns pulsed electric fields. *IEEE transactions on dielectrics and electrical insulation*. 2017;24:3985-3994

[9] de Caro, A., Bellard, E., Kolosnjaj-Tabi, J., Golzio, M., & Rols, M. (2023). **Gene** electrotransfer efficiency in 2D and 3D cancer cell models using different electroporation protocols: A comparative study. *Pharmaceutics, 15*(3), 1004. https://doi.org/10.3390/pharmaceutics15031004

[10] Leguèbe, M., Notarangelo, M. G., Twarogowska, M., Natalini, R., & Poignard, C. (2017). Mathematical model for transport of DNA plasmids from the external medium up to the nucleus by electroporation. *Mathematical Biosciences, 285*, 1-13. https://doi.org/10.1016/j.mbs.2016.11.015

[11] Towbin JA, McKenna WJ, et al. 2019 HRS expert consensus statement on evaluation, risk stratification, and management of arrhythmogenic cardiomyopathy. *Heart Rhythm* 2019, 16(11):e301–e372

[12] Arytmogenní kardiomyopatie. In: *WikiSkripta* [online]. [cit. 2025-06-27]. Dostupné z: Arytmogenní kardiomyopatie — WikiSkripta

[13] KAUTZNER, Josef. *Srdeční selhání : aktuality pro klinickou praxi.* - vydání. Mladá fronta, 2015. ISBN 9788020435736

[14] CORRADO, Domenico, Cristina BASSO a Daniel P. JUDGE. Arrhythmogenic Cardiomyopathy. *Circulation Research.* 2017, roč. 7, vol. 121, s. 784-802, ISSN 0009-7330. DOI: 10.1161/circresaha.117.309345

[15] Arrhythmogenic cardiomyopathy (ACM). In: *Penn Medicine*[online]. Philadelphia, PA 800-789-7366 © 2025, The Trustees of the University of Pennsylvania. Dostupné z: Arrhythmogenic Cardiomyopathy | Penn Medicine

Analysis of auditory stem responses in healthy subjects and cochlear implant patients using BERA and eABR methods

Andrea Šilhábelová

Hearing is a sensory organ, crucial for spatial orientation, communication and psychosocial development. Its impairment can significantly affect quality of life, especially in children, where it has a major impact on language and social skills. Hearing parameters can be determined by numerous tests, including objective audiometric methods such as *BERA* (*Brainstem Evoked Response Audiometry*) and *eABR* (*Electrical Auditory Brainstem Response*), which provide valuable information about function of the auditory nerve and auditory brainstem pathway.

The main objective of this work was to compare auditory brainstem response of healthy population with population of patients with cochlear implants. The work was carried out in collaboration with the ORL clinic at the University Hospital in Motol using the *GSI Audera Pro* device. The *frequency non-specific BERA* method was performed with acustic stimulus *click* on a sample of 5 probands and the *frequency specific BERA* method using a *tone-burst* stimulus on a sample of 10 probands. On a sample of 3 probands with cochlear implants, the *eABR* method was performed using electrical stimulation.

The results show that in healthy population age does not affect the analyzed parameters of *absolute latencies* and *wave amplitudes* for the considered Jewett waves III and V. On a sample of 5 probands no significant difference was found in the statistical evaluation between the analyzed parameters obtained by *frequency non-specific* and *frequency specific BERA* methods. Comparison of the *frequency-nonspecific BERA* and *eABR* methods shows that electrical stimulation leads to shorter *absolute latencies* (on average 0.77 ms for Jewett wave III and 1.28 ms for Jewett wave V) and higher *wave amplitudes* (on average 0.44 μV for Jewett wave III and 0.54 μV for Jewett wave V). The results further suggest statistically significant differences between the methods at stimulation electrodes 1 and 4, whereas the responses captured by the methods at electrode 2 are identical.

Keywords

Auditory evoked potentials; *frequency non-specific BERA* method; *frequency specific BERA* method; *eABR* method; *absolute wave latencies*; *wave amplitude*

Temperature Monitoring During Superficial Hyperthermia in the Neck Area Using Microwave Imaging

Barbora Smahelova[1], Jakub Kollar[1], Ondrej Fiser[1], and Jan Vrba[1]

[1]Department of Biomedical Engineering, Czech Technical University in Prague,
27201 Prague, Czech Republic

August 24, 2025

Abstract

This study explores the application of microwave imaging (MWI) for temperature monitoring during hyperthermia therapy in the neck region. An anthropomorphic neck model was developed, combined with a model of a clinically used hyperthermia applicator, and the temperature distribution was calculated. A contrast region representing heated tissue was introduced and reconstructed via MWI using the Born approximation (BA). The three MWI configurations of the antenna array tested successfully detected the contrast region, with the optimal configuration achieving sensitivity 82% and specificity 72%. These findings provide a basis for future experimental validation.

1 Introduction

Cancer remains one of the most significant global health challenges and is one of the leading causes of death worldwide. The GLOBOCAN analysis reported more than 18 million new cases and over 9 million deaths in 2022 [1]. Head and neck cancers (HNC), encompassing malignancies of the lips, oral cavity, salivary glands, pharynx, and larynx, represent a major subgroup. In 2022, nearly 900,000 new cases of HNC were diagnosed and more than 500,000 deaths were recorded [1]. Although standard treatment strategies include surgery, radiotherapy, chemotherapy, or their combination, many patients are diagnosed in advanced stages when the prognosis is poor [2]. This highlights the need for better therapeutic approaches.

Hyperthermia (HT) has been investigated as an effective adjuvant method to conventional cancer therapies. By raising the tumour temperature to 40–44 °C, HT can enhance the effects of radiotherapy and chemotherapy [3, 4]. Clinical studies have shown that combining radiotherapy with HT improves local tumour control and survival without significantly increasing toxicity [5]. Different treatment strategies exist, including local, regional, and whole-body HT, with energy delivered using microwaves, radiofrequency, or ultrasound [6, 7]. Microwave-based systems are particularly promising because of their ability to heat deep-seated tissues with controlled energy deposition.

A critical factor in HT therapy is accurate thermometry, which ensures that therapeutic temperatures are reached in the target region while avoiding damage to healthy tissue [8]. Conventional invasive probes provide reliable point measurements, but are associated with patient discomfort and the risk of complications [9]. Non-invasive methods such as magnetic resonance imaging or ultrasound offer spatially resolved monitoring, yet they remain limited by cost, compatibility, or technical constraints. Microwave imaging (MWI) has recently emerged as a promising non-invasive technique, offering real-time monitoring and integration with existing HT systems [10, 11].

The interaction of microwaves with biological tissues is governed by their dielectric properties, which depend on both frequency and temperature [12, 13]. This relationship enables microwaves not only to deliver therapeutic heating but also to provide diagnostic and monitoring capabilities. Recent advances in signal processing and inverse reconstruction methods have further improved the feasibility of microwave-based thermometry and imaging in clinical applications [14, 15].

The main aim of this work is to evaluate the feasibility of MWI for temperature monitoring during superficial microwave HT in the head and neck region. A simplified anatomical model of the patient's neck is developed with a Beta HT applicator (MED-LOGIX SRL, Italy) and the induced temperature field is simulated. The tissue dielectric parameters are adjusted according to the temperature, and three antenna configurations are tested to reconstruct temperature-related contrast changes using differential MWI on synthetic simulation data.

2 Methods

2.1 Hyperthermia Simulation

Electromagnetic simulations were performed in *Sim4Life* (Med Tech, Zürich, Switzerland) [16], based on the finite difference time domain (FDTD) method. The computational domain was discretised into a grid, Maxwell's equations were solved in the time domain, and the fields were subsequently transformed into the frequency domain via Fourier transform.

For microwave HT, a 2.5D patient model was derived from the DUKE v3.1.1 Slice Model [17], using a transverse section at the level of the C5 vertebra (Fig. 1a). From the plane, the relevant anatomical structures were selected and extruded to a height of 20 cm (Fig. 1b). A Beta HT applicator with a water bolus was placed on the surface to provide efficient cooling and microwave coupling (Fig. 1c). The excitation frequency was set to 434 MHz, following clinical practice.

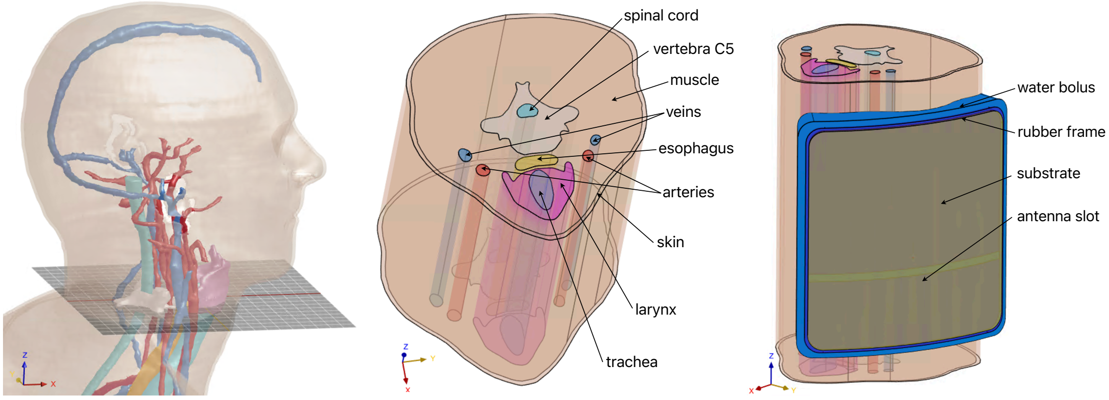

(a) (b) (c)

Figure 1: Duke model: (a) slicing plane at the C5, (b) 2.5D neck model

The dielectric and thermal properties of the tissues were taken from the IT'IS database [18]. Heat generation in tissues included electromagnetic absorption q_{EM} and perfusion exchange q_{BP}:

$$q = q_{EM} + q_{BP}, \qquad q_{EM} = \tfrac{1}{2}\sigma|E|^2, \qquad q_{BP} = -\rho_B C_B \omega_B (T - T_a). \tag{1}$$

The initial temperatures were defined as 37 °C for tissue, 30 °C for the water bolus, and 25 °C for ambient air.

2.2 Microwave Imaging Simulations

Dielectric properties were modeled using the single-pole Cole–Cole model [19]:

$$\varepsilon(\omega, \vartheta) = \varepsilon_\infty(\vartheta) + \frac{\Delta\varepsilon_1(\vartheta)}{1 + (j\omega\tau(\vartheta))^{1-\alpha}} - j\frac{\sigma_s(\vartheta)}{\omega\varepsilon_0}. \tag{2}$$

These parameters were experimentally measured in [19] and are shown in Fig. 2. Based on hyperthermia simulations (Sec. 3.1), the 44 °C isocontour (see Fig. 6) was used to define the contrast region for steady-state MWI simulations (see the black contrast region in Fig. 3). For MWI simulations, ultra-wideband (UWB) bowtie antennas, designed specifically for biomedical microwave imaging applications, as presented in [14, 20]. The antenna is optimised for the frequency band of 1–6 GHz and excels in high radiation efficiency, symmetrical radiation pattern, low backward radiation, and short impulse response. UWB antennas were used at 1 GHz (based on the results of [19]), selected as a trade-off between dielectric sensitivity and propagation losses. Table 1 lists

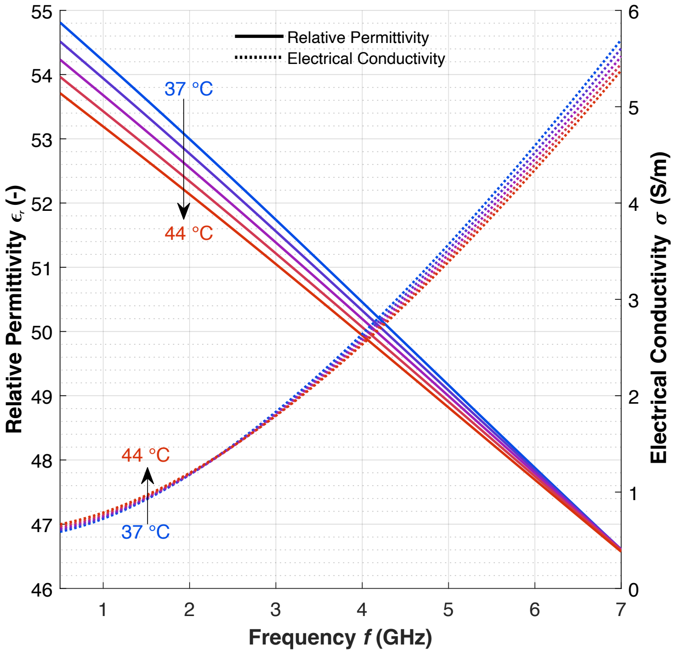

Figure 2: Frequency dependence of muscle dielectric parameters at different temperatures [19].

the dielectric parameters at 1 GHz of muscle tissue at baseline (T_0) and steady-state (T_{stac}). The true dielectric contrast, corresponding to a temperature increase of 7 °C, was $\Delta\epsilon_r = -1.02$ and $\Delta\sigma = +0.064$ S/m.

	T_0		T_{stac}	
Temperature	ε_r (−)	σ (S/m)	ε_r (−)	σ (S/m)
37 °C	54.21	0.723	54.21	0.723
44 °C	54.21	0.723	53.19	0.787

Table 1: Dielectric parameters of muscle tissue at 1 GHz for differential MWI.

MWI models are shown in Fig. 4. For each, two simulations were run to get S-matrices: baseline (S_{T0}) and steady-state (S_{stac}). White Gaussian noise ($SNR = 80$ dB) was added to approximate experimental conditions. Three antenna array configurations were tested:

- Configuration 1: 19 antennas in 2 planes with vertical polarization,
- Configuration 2: 24 antennas in 3 planes with vertical polarization,
- Configuration 3: 22 antennas in 5 planes with horizontal polarization,

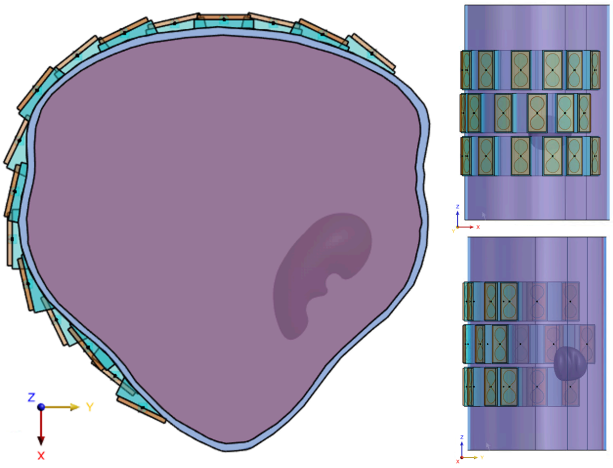

Figure 3: Example MWI model (configuration 2) with contrast region indicated in black.

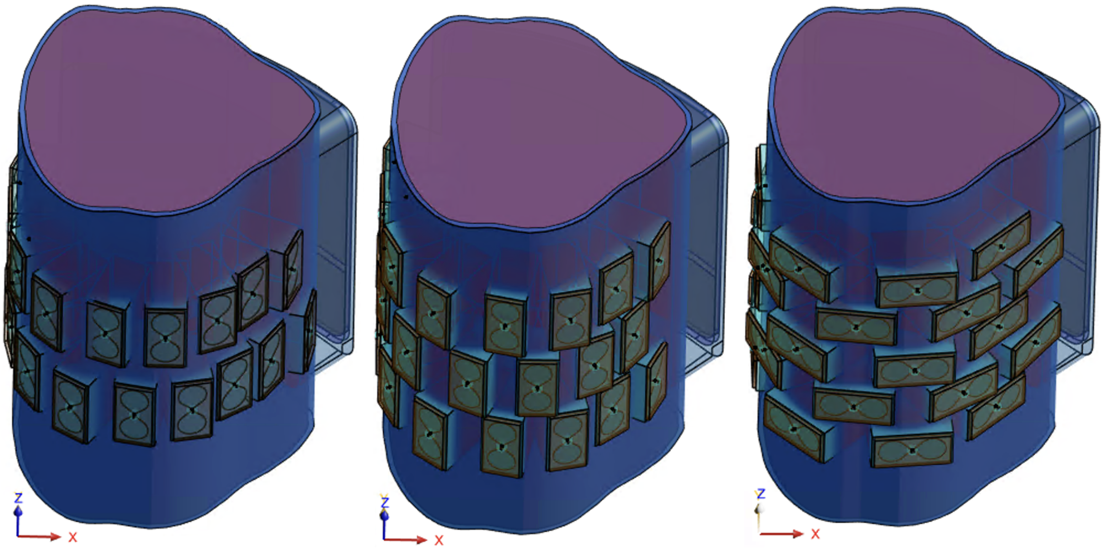

(a) Configuration 1 (19 antennas, 2 planes).

(b) Configuration 2 (24 antennas, 3 planes).

(c) Configuration 3 (22 antennas, 5 planes).

Figure 4: Different antenna configurations for MWI models.

2.3 Reconstruction and Evaluation

Differential S-parameters were defined as

$$\Delta S_{norm} = \frac{S_{stac} - S_{T0}}{S_{T0}}, \tag{3}$$

with Born approximation ($E_{tot} \approx E_{inc}$) and TSVD regularization:

$$\delta O = \sum_{n=1}^{N_{TSVD}} \frac{1}{\sigma_n} \langle \Delta S, U_n \rangle V_n, \tag{4}$$

where δO relates to permittivity and conductivity as

$$\delta O = \varepsilon_0 \Delta \varepsilon_r - \frac{j}{\omega} \Delta \sigma. \tag{5}$$

Reconstructed images were binarized and compared to the ground-truth contrast region. Performance was evaluated with Dice Similarity Coefficient (DSC),

$$DSC = \frac{2TP}{2TP + FP + FN}, \tag{6}$$

Matthews Correlation Coefficient (MCC),

$$MCC = \frac{TP \cdot TN - FP \cdot FN}{\sqrt{(TP + FP)(TP + FN)(TN + FP)(TN + FN)}}, \tag{7}$$

and sensitivity and specificity:

$$sensitivity = \frac{TP}{TP + FN}, \qquad specificity = 1 - \frac{FP}{TP + FP}. \tag{8}$$

3 Results

3.1 Hyperthermia

The hyperthermia simulations yielded the spatial temperature distribution within the patient model, shown in Fig. 5. From this distribution, isothermal contours ranging from 38 °C to 44 °C with 1 °C increments were extracted (Fig. 6). The isocontour corresponding to 44 °C (Fig. 3) was subsequently used as the contrast region for MWI (described in Sec. 2.2).

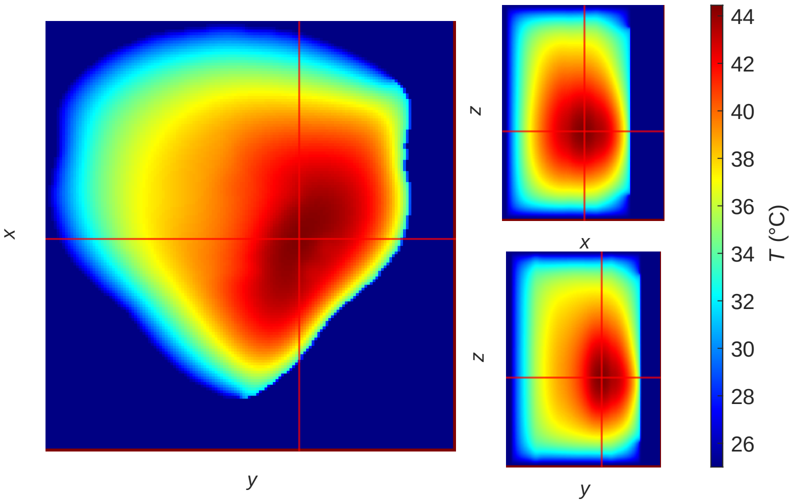

Figure 5: Simulated temperature distribution.

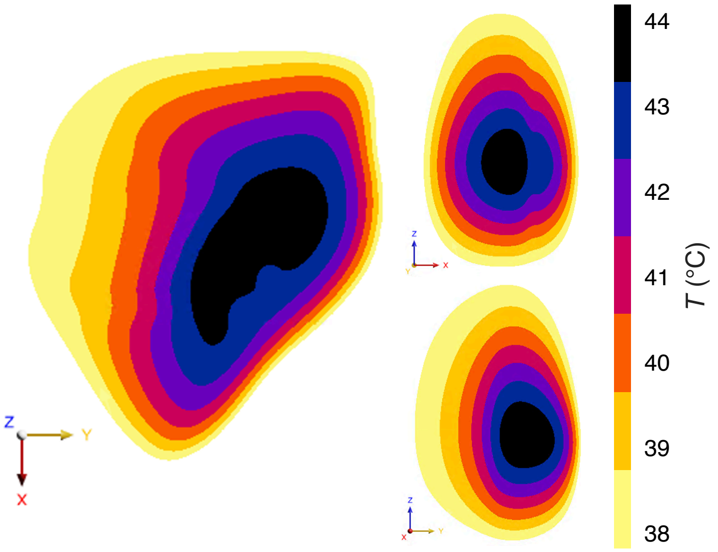

Figure 6: Extracted temperature isocontours.

3.2 Microwave Imaging

The objective of the antenna field deployment analysis was to obtain optimal antenna deployment to maximize the qualitative and quantitative parameters of the reconstructions described in Sec. 2.3.

Fig. 7 presents reconstructions for individual configurations in triplanar view with identical colour scaling. For clarity, reconstructions of the absolute value of complex permittivity $|\Delta\varepsilon|$ were evaluated. The MWI reconstructions were co-registered and fused with the mask of the actual contrast region, which corresponded to the 44 °C isocontour. Individual reconstructions were evaluated on the basis of qualitative metrics (reported in Table 2). From the image reconstructions and evaluation parameters, it can be observed that configurations 1 and 2 (vertical polarisation) exhibit better values than configuration 3 (horizontal polarization).

Configuration	Sensitivity (%)	Specificity (%)	DSC (–)	MCC (–)
1 (19 antennas, 2 planes)	80	74	0.77	0.77
2 (24 antennas, 3 planes)	82	72	0.77	0.77
3 (22 antennas, 5 planes)	80	67	0.73	0.74

Table 2: Qualitative evaluation of reconstructions.

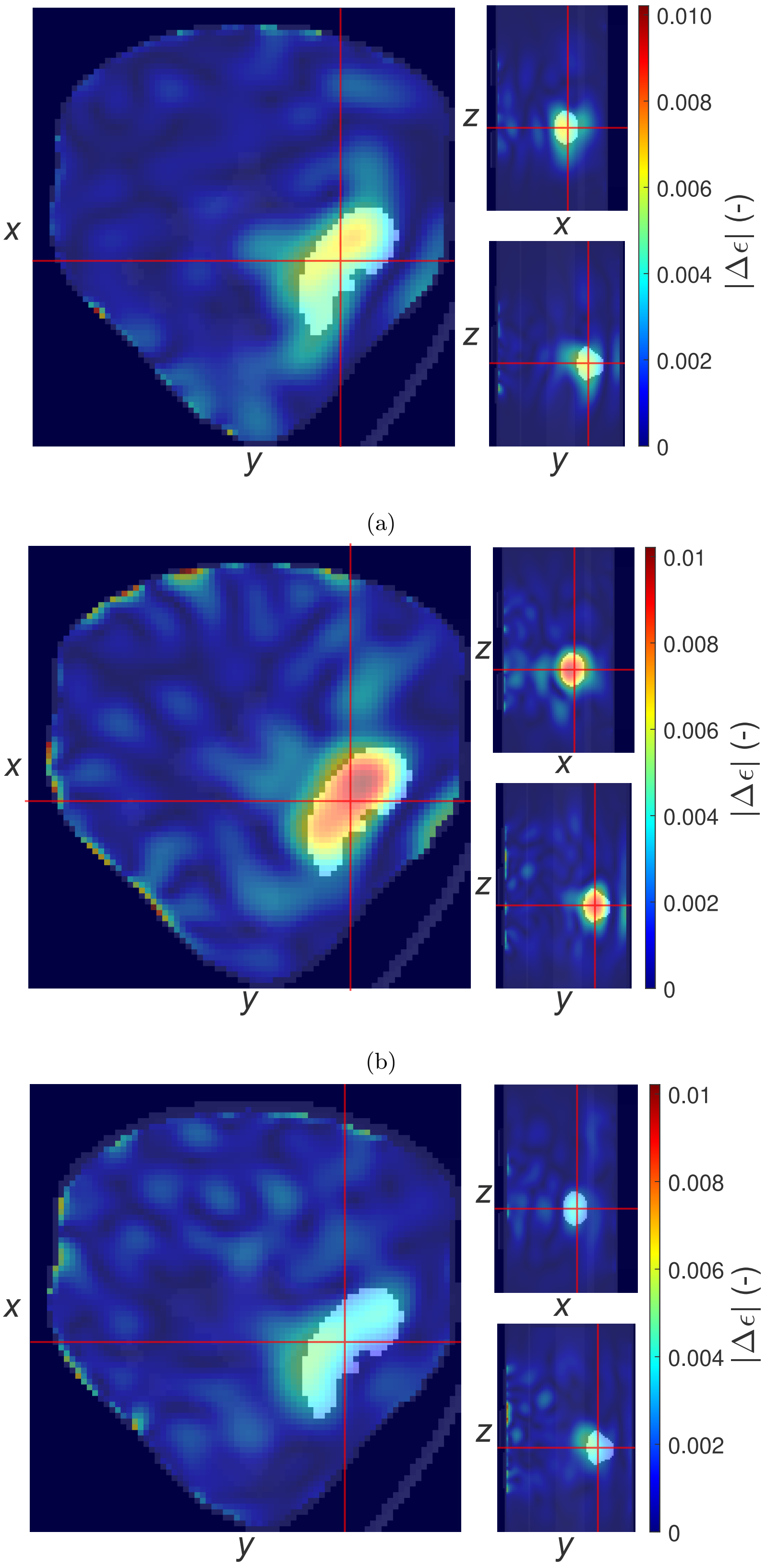

(a)

(b)

(c)

Figure 7: Antenna deployment reconstructions: (a) Configuration 1, (b) Configuration 2, (c) Configuration 3

4 Discussion

This study numerically confirmed the feasibility of using MWI for temperature monitoring during HT treatment in the neck region.

The HT system model was heterogeneous and incorporated different tissue types with their respective thermal and dielectric properties. The goal was to realistically capture the temperature distribution during therapeutic heating. For a more realistic scenario, a full 3D neck model would be preferable over the current 2.5D model. In addition, not all neck tissues were included, such as neural structures or lymph nodes.

Consistent with clinical practice, the simulations used a single HT applicator operating at 434 MHz. This setup, typical for superficial HT in the head and neck, limits control of the temperature field, as the adjustable parameters include only power, frequency, and exposure time. Using multiple applicators would allow for targeted heating via superposition of electromagnetic fields. However, head and neck tumours are often superficial, allowing effective heating with a single applicator positioned over the tumour.

For MWI, a homogeneous muscle equivalent model was used. This approach isolated the effect of temperature changes on the dielectric properties, without complications from structural heterogeneity.

The reconstructed contrast included only the smallest volume temperature isocontour, i.e., the region with the highest temperature increase. Reconstructions therefore captured only the most pronounced part of the temperature field, maximising detectable contrast and simplifying the inverse problem. Future work should aim to reconstruct all temperature isocontours with corresponding dielectric properties.

Three antenna configurations were evaluated for MWI: 19 antennas in two planes, 24 antennas in three planes, and 22 antennas in five planes. In the last configuration, antennas were additionally rotated by 90 ° (horizontal polarisation), imposing spatial constraints and preventing an increase in antenna count despite the additional planes. The results suggest that the horizontal orientation of the antenna is not preferable to vertical polarisation.

The number of antennas per configuration was determined by spatial limitations and the maximum number of ports available on the ZNB 8 vector network analyser (VNA, Rohde&Schwarz). The switching matrix used has 24 ports, setting the practical limit for the antenna count. From a practical and clinical perspective, the height of the system must match the anatomy of the patient's neck. In this regard, the two-plane configuration with vertical polarisation appears to be most suitable due to its minimal height and highest potential for real-world application. However, it is limited by the number of antennas per plane; increasing antenna count would require closer spacing, potentially degrading interactions, and reconstruction quality.

Despite differences in antenna count and spatial arrangement, reconstruction quality was comparable in all configurations. All configurations reliably detected the contrast region, demonstrating that smaller antenna arrays can be effective if properly designed.

In conclusion, this work highlights the potential of MWI for HT monitoring. The numerical results were made more realistic by adding additive noise ($SNR = 80$ dB), approximating the experimental conditions. The qualitative results suggest that the proposed approach is feasible. Future research should validate the method on more realistic anatomical models, followed by physical phantoms, and focus on reconstruction robustness under noisy conditions.

5 Conclusion

The simplified anatomical neck model, combined with an HT applicator, was used for simulations of therapeutic HT and MWI. During simulations, the safe temperature limit of 45 °C was not exceeded, while the region above 44 °C was used as contrast area for imaging purposes. Testing three different antenna field configurations for MWI demonstrated the ability to reconstruct the contrast region with a sensitivity of 80–82 % and a specificity of 67–74 %. These results confirm the suitability of the proposed system for further research and development in non-invasive diagnostics and therapy using microwave technologies. Experimental measurements will be conducted in the follow-up work to validate the numerical results and confirm the practical applicability of the system.

References

1. BRAY, Freddie; LAVERSANNE, Mathieu; SUNG, Hyuna; FERLAY, Jacques; SIEGEL, Rebecca L.; SOERJOMATARAM, Isabelle; JEMAL, Ahmedin. Global cancer statistics 2022: GLOBOCAN estimates of incidence and mortality worldwide for 36 cancers in 185 countries. *CA: A Cancer Journal for Clinicians* [online]. 2024, vol. 74, no. 3, pp. 229–263 [visited on 2025-03-06]. ISSN 0007-9235, ISSN 1542-4863. Available from DOI: `10.3322/caac.21834`. Number: 3.
2. JOHNSON, Daniel E.; BURTNESS, Barbara; LEEMANS, C. René; LUI, Vivian Wai Yan; BAUMAN, Julie E.; GRANDIS, Jennifer R. Head and neck squamous cell carcinoma. *Nature Reviews Disease Primers* [online]. 2020, vol. 6, no. 1, p. 92 [visited on 2025-03-06]. ISSN 2056-676X. Available from DOI: `10.1038/s41572-020-00224-3`. Number: 1.
3. WUST, P; HILDEBRANDT, B; SREENIVASA, G; RAU, B; GELLERMANN, J; RIESS, H; FELIX, R; SCHLAG, Pm. Hyperthermia in combined treatment of cancer. *The Lancet Oncology* [online]. 2002, vol. 3, no. 8, pp. 487–497 [visited on 2025-03-08]. ISSN 14702045. Available from DOI: `10.1016/S1470-2045(02)00818-5`. Number: 8.
4. CREZEE, Hans; CASPAR M. VAN LEEUWEN; OEI, Arlene L.; STALPERS, Lukas J.A.; BEL, Arjan; FRANKEN, Nicolaas A.; KOK, H. Petra. Thermoradiotherapy planning: Integration in routine clinical practice. *International Journal of Hyperthermia* [online]. 2016, vol. 32, no. 1, pp. 41–49 [visited on 2025-03-08]. ISSN 0265-6736, ISSN 1464-5157. Available from DOI: `10.3109/02656736.2015.1110757`. Number: 1.
5. VALDAGNI, Riccardo; AMICHETTI, Maurizio. Report of long-term follow-up in a randomized trial comparing radiation therapy and radiation therapy plus hyperthermia to metastatic lymphnodes in stage IV head and neck patients. *International Journal of Radiation Oncology*Biology*Physics* [online]. 1994, vol. 28, no. 1, pp. 163–169 [visited on 2025-03-07]. ISSN 03603016. Available from DOI: `10.1016/0360-3016(94)90154-6`. Number: 1.
6. TREFNÁ, Hana Dobšíček; CREZEE, Hans; SCHMIDT, Manfred; MARDER, Dietmar; LAMPRECHT, Ulf; EHMANN, Michael; HARTMANN, Josefin; NADOBNY, Jacek; GELLERMANN, Johanna; VAN HOLTHE, Netteke; GHADJAR, Pirus; LOMAX, Nicoletta; ABDEL-RAHMAN, Sultan; BERT, Christoph; BAKKER, Akke; HURWITZ, Mark D.; DIEDERICH, Chris J.; STAUFFER, Paul R.; VAN RHOON, Gerard C. Quality assurance guidelines for superficial hyperthermia clinical trials: I. Clinical requirements. *International Journal of Hyperthermia* [online]. 2017, vol. 33, no. 4, pp. 471–482 [visited on 2025-03-26]. ISSN 0265-6736, ISSN 1464-5157. Available from DOI: `10.1080/02656736.2016.1277791`. Number: 4.
7. VAN DER ZEE, J. Heating the patient: a promising approach? *Annals of Oncology* [online]. 2002, vol. 13, no. 8, pp. 1173–1184 [visited on 2025-03-26]. ISSN 09237534. Available from DOI: `10.1093/annonc/mdf280`. Number: 8.
8. DE BRUIJNE, Maarten; VAN DER ZEE, Jacoba; AMEZIANE, Ali; VAN RHOON, Gerard C. Quality control of superficial hyperthermia by treatment evaluation. *International Journal of Hyperthermia* [online]. 2011, vol. 27, no. 3, pp. 199–213 [visited on 2025-04-02]. ISSN 0265-6736, ISSN 1464-5157. Available from DOI: `10.3109/02656736.2010.525226`.
9. WUST, Peter; CHO, Chie Hee; HILDEBRANDT, Bert; GELLERMANN, Johanna. Thermal monitoring: Invasive, minimal-invasive and non-invasive approaches. *International Journal of Hyperthermia* [online]. 2006, vol. 22, no. 3, pp. 255–262 [visited on 2025-04-02]. ISSN 0265-6736, ISSN 1464-5157. Available from DOI: `10.1080/02656730600661149`.
10. HAYNES, Mark; STANG, John; MOGHADDAM, Mahta. Real-time Microwave Imaging of Differential Temperature for Thermal Therapy Monitoring. *IEEE Transactions on Biomedical Engineering* [online]. 2014, vol. 61, no. 6, pp. 1787–1797 [visited on 2025-04-02]. ISSN 0018-9294, ISSN 1558-2531. Available from DOI: `10.1109/TBME.2014.2307072`.
11. PROKHOROVA, Alexandra; LEY, Sebastian; HELBIG, Marko. Quantitative Interpretation of UWB Radar Images for Non-Invasive Tissue Temperature Estimation during Hyperthermia. *Diagnostics* [online]. 2021, vol. 11, no. 5, p. 818 [visited on 2025-04-02]. ISSN 2075-4418. Available from DOI: `10.3390/diagnostics11050818`.

12. GABRIEL, S; LAU, R W; GABRIEL, C. The dielectric properties of biological tissues: II. Measurements in the frequency range 10 Hz to 20 GHz. *Physics in Medicine and Biology* [online]. 1996, vol. 41, no. 11, pp. 2251–2269 [visited on 2025-04-08]. ISSN 0031-9155, ISSN 1361-6560. Available from DOI: `10.1088/0031-9155/41/11/002`.
13. LAZEBNIK, Mariya; POPOVIC, Dijana; MCCARTNEY, Leah; WATKINS, Cynthia B; LINDSTROM, Mary J; HARTER, Josephine; SEWALL, Sarah; OGILVIE, Travis; MAGLIOCCO, Anthony; BRESLIN, Tara M; TEMPLE, Walley; MEW, Daphne; BOOSKE, John H; OKONIEWSKI, Michal; HAGNESS, Susan C. A large-scale study of the ultrawideband microwave dielectric properties of normal, benign and malignant breast tissues obtained from cancer surgeries. *Physics in Medicine and Biology* [online]. 2007, vol. 52, no. 20, pp. 6093–6115 [visited on 2025-04-08]. ISSN 0031-9155, ISSN 1361-6560. Available from DOI: `10.1088/0031-9155/52/20/002`.
14. FISER, Ondrej; HRUBY, Vojtech; VRBA, Jan; DRIZDAL, Tomas; TESARIK, Jan; VRBA JR, Jan; VRBA, David. UWB Bowtie Antenna for Medical Microwave Imaging Applications. *IEEE Transactions on Antennas and Propagation* [online]. 2022, vol. 70, no. 7, pp. 5357–5372 [visited on 2025-06-06]. ISSN 0018-926X, ISSN 1558-2221. Available from DOI: `10.1109/TAP.2022.3161355`.
15. ASOK, Athul O.; S. J., Gokul Nath; DEY, Sukomal. Monostatic microwave imaging of cancerous breast phantom with a frequency to time domain conversion technique. *Microwave and Optical Technology Letters* [online]. 2024, vol. 66, no. 2, e34054 [visited on 2025-04-08]. ISSN 0895-2477, ISSN 1098-2760. Available from DOI: `10.1002/mop.34054`.
16. *Sim4Life*. Zurich, Švýcarsko: MedTech, [n.d.].
17. *DUKE cV3-1 » IT'IS Foundation*. [N.d.]. Available also from: `https://itis.swiss/virtualpopula%20tion/virtua%20l-popula%20tion/vip3/duke/duke%20-cv3-1/`.
18. IT'IS FOUNDATION. *Tissue Properties Database V4.2* [online]. In collab. with IT'IS FOUNDATION. IT'IS Foundation, 2024 [visited on 2025-06-18]. Available from DOI: `10.13099/VIP21000-04-2`.
19. LEY, Sebastian; SCHILLING, Susanne; FISER, Ondrej; VRBA, Jan; SACHS, Jürgen; HELBIG, Marko. Ultra-Wideband Temperature Dependent Dielectric Spectroscopy of Porcine Tissue and Blood in the Microwave Frequency Range. *Sensors* [online]. 2019, vol. 19, no. 7, p. 1707 [visited on 2025-02-28]. ISSN 1424-8220. Available from DOI: `10.3390/s19071707`. Number: 7.
20. KOLLAR, Jakub; NOVAK, Marek; BABAK, Milan; DRIZDAL, Tomas; VRBA, Jan; VRBA, David; POKORNY, Tomas; LINHA, Zdenek; FISER, Ondrej. Potential of UWB Radar Systems in Monitoring Liver Ablation: A Phantom Model Study. *IEEE Transactions on Antennas and Propagation* [online]. 2024, pp. 1–1 [visited on 2025-04-08]. ISSN 0018-926X, ISSN 1558-2221. Available from DOI: `10.1109/TAP.2024.3513555`.

FBME CTU
BioEM group

Simulation of conventional gradient coils for a low-field magnetic resonance system

Author: Vilém Fojtík
Supervisor: prof. Ing. David Vrba, Ph.D.

Abstract

This project focuses on design and simulation of conventional gradient coils for a low-field magnetic resonance system. The requirement of the assignment was to achieve a gradient at the centre of the magnetic field of at least 5 mT/m at a current of 15 A. The CoilGen program was used to design the coils and generate 3D models in .stl format. These models were then converted to .txt format so that they could be imported into the COMSOL Multiphysics simulation environment. The simulations verified the functionality of the design and provided the basis for calculating the resulting magnetic field gradients for each axis. The resulting gradients in the center of the field were 5.84 mT/m (X-axis coil), 25.97 mT/m (Y-axis coil) and 18.69 mT/m (Z-axis coil).

The Y-axis coil was physically manufactured beyond the original assignment. This coil was produced using 3D printing, hand wound and then measured. The resistance was determined using the four-square method and using an RLC meter, where the inductance of the coil was also determined. The magnetic induction was measured with a teslameter. The resulting gradient in the center of the field was 12.8 mT/m.

1. INTRODUCTION

Currently, the most advanced clinical MR devices in developed countries are in high demand and unavailable in many developing countries. This is mainly due to their high manufacturing and operating costs. Patients often have to wait several months for an examination. Due to the long waiting times, it can sometimes be too late to start treatment.

According to the World Health Organization, the Czech Republic had 10.27 MR devices per one million inhabitants between 2017 and 2019. During the same period, Colombia had around 0.24 devices for the same number of inhabitants. [1]

Due to the lower production and operating costs of low-field MR devices and their smaller size, it will be possible to increase their number. [2] The costs of these devices should be under approximately 50 000 €. [3]

2. METHODS

2.1 Model creation

In order to create a model is important to start with setting up a target gradient magnetic field, according to which the model is subsequently calculated and optimized. The shape of the target gradient magnetic field, in short the target field, is a sphere with a radius of 0.125 m.

The model was created using the CoilGen program, which was developed in the Matlab environment. It consists of two main parts, namely the CoilGen function and the Linear_GradientCoil code, which uses the CoilGen function to create conventional gradient coils and then to save it as mesh structure. For an example, Figure 2.1 shows the mesh structure of the coil for the Z-axis.

This mesh structure creates a form for laying out the path of the conductor in the tube, which will serve as the conductor carrier. After setting the required parameters and running the program, the calculation of the mesh structure of the coils takes place, which sometimes takes several hours. The result is generated conductor paths stored in the form of an .stl file.

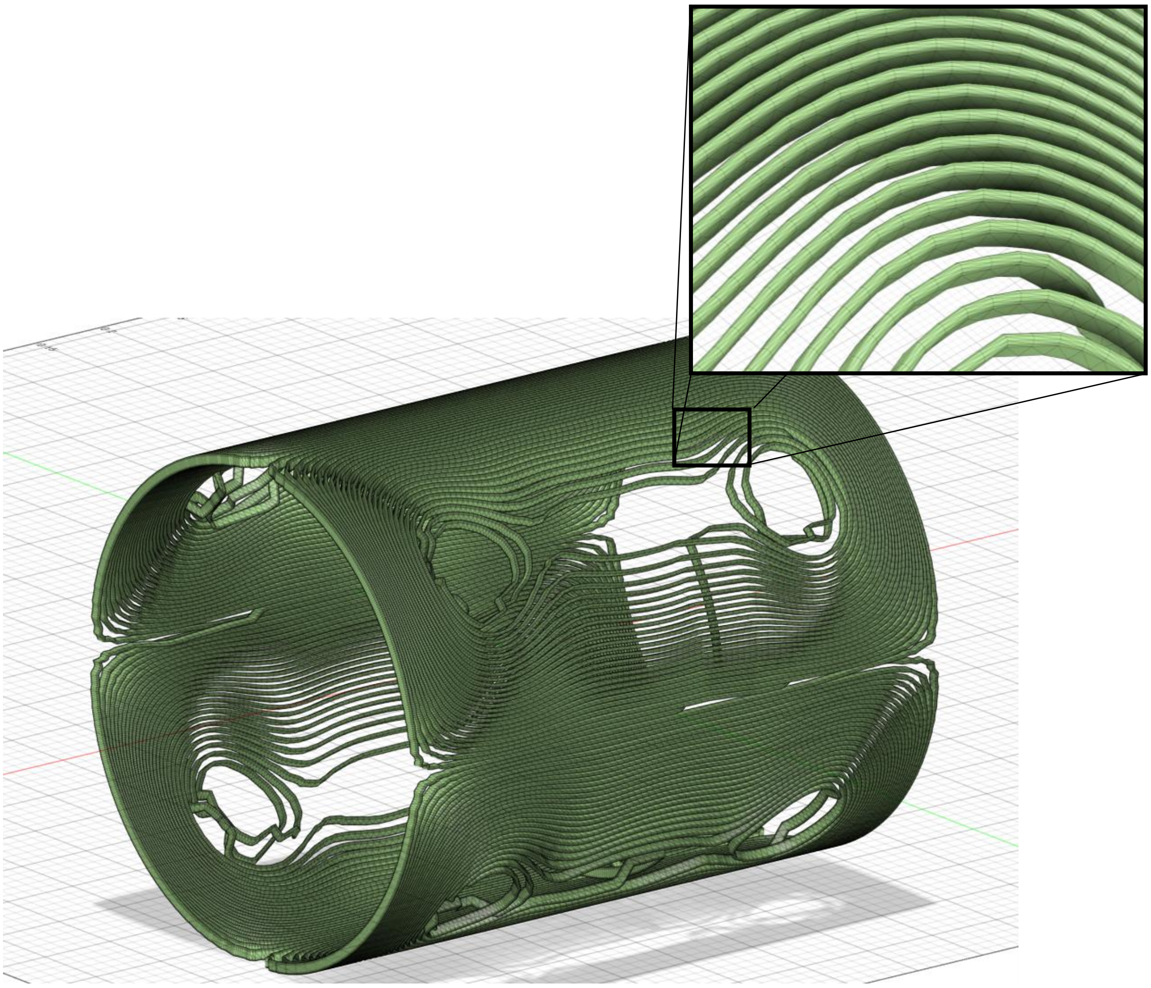

Figure 2.1: Mesh structure for coil in Z axis

2.2 Model modification

The files created in the previous chapter (2.1 Model Creation) in .stl format could not be uploaded and correctly loaded in the COMSOL Multiphysics environment. For this reason, it was necessary to rewrite the file to .txt format. This modification was performed in the Matlab environment. The structure of the .stl file, which consists of points located at the vertices of triangles and information about the order of their connections, was used to create the text document. Thanks to this knowledge, it was possible to write down and sort all the points. The written and sorted points then had to be recalculated so that they only represented the curve of the conductor forming the coil and not the form for carving out. To recalculate the points, it was necessary to know the shape in which the points were arranged. For each coil, a set of 72 points corresponding to six cross-sections, each with 12 points, was selected, see Figure 2.2. The calculated averages were written down in a text document and then entered into COMSOL Multiphysics.

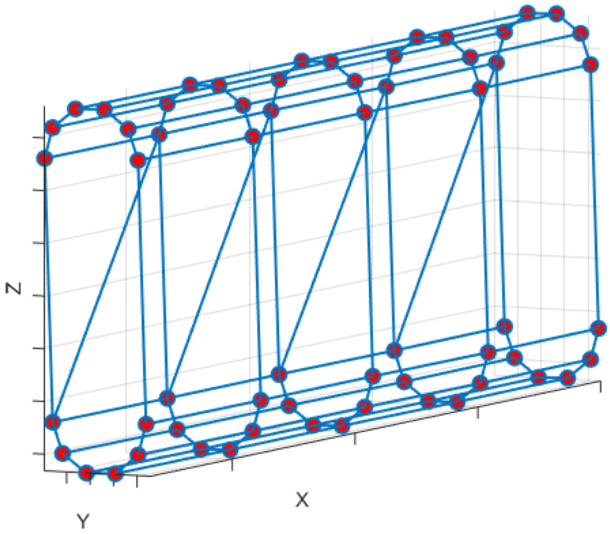

Figure 2.2: Structure of the coil mesh shape

2.3 Model simulation in COMSOL Multiphysics

The coil models were simulated in COMSOL Multiphysics, where each coil was simulated separately. The reason for this was the high computational capacity required by the model and the desire to determine the electromagnetic properties of the individual coils. Geometry was imported as an interpolation curve. As physics were used magnetic fields. Simulations were computed in stationary and also frequency domain, where was frequency setup for 10 kHz and current of 15 A.

The results were processed using the cutline function, which made it possible to plot a graph of the magnetic field strength as a function of distance. These cutlines were drawn depending on the axis of the coil's action. The gradient of individual areas was calculated manually using the magnetic field gradient formula:

$$G = \frac{\Delta B}{\Delta s} \tag{2.1}$$

where *ΔB* is the change in magnetic induction and *Δs* is the distance over which the change occurs. All cutlines were drawn in the center of the field parallel to the axis of the fields formed by a specific coil.

2.4 Production and measurement of the gradient coil created for the Y-axis

The template for the coil was created on a PrushaXL 3D printer using PETG material. Litz wire (a bundle of copper wires with a lacquer coating) was wound into the template to serve as a conductor. This type of conductor was chosen because the composition of many smaller wires is advantageous both in terms of wire resistance while maintaining its overall width and in terms of the so-called skin effect. Resistance is inversely proportional to the cross-sectional area of the conductor, and the skin effect refers to the depth to which the flowing current penetrates depending on the frequency of the alternating current. After the coil was completely wound, it was connected to a four-terminal circuit to measure its resistance with 9.3 A. The coil was then connected to an RLC meter, where its inductance was measured and its resistance was also remeasured. The last measurement was made by teslameter perpendicular to the main loop, with 1 cm spacing. The placement was as similar as possible as it was in the simulations. The current floating through the circuit was 10.05 A.

3. RESULTS

3.1 Coil Models

Figures 3.1, 3.2 and 3.3 show the models of gradient coils designed for primary action along the X, Y and Z axes. All simulations and calculations were performed on these created models.

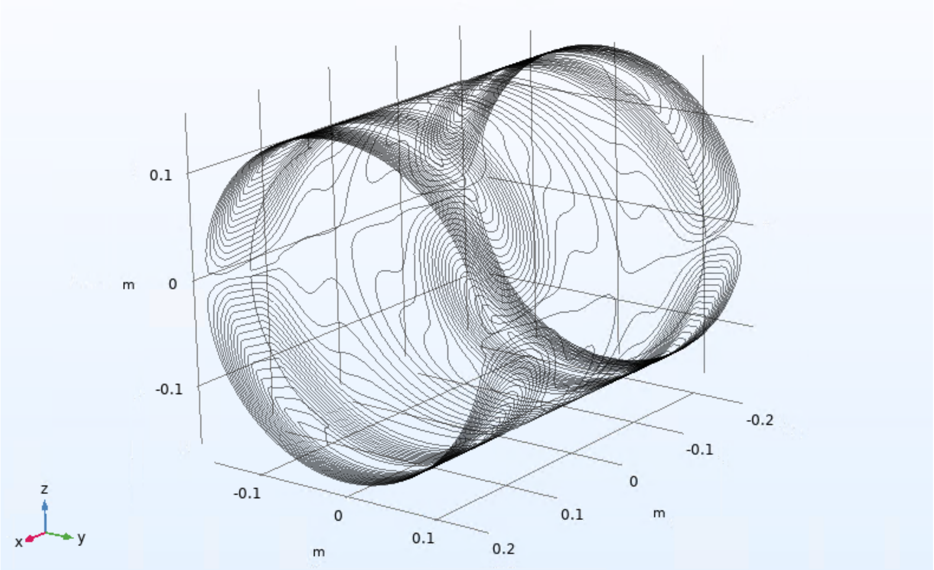

Figure 3.1: Coil for the X-axis

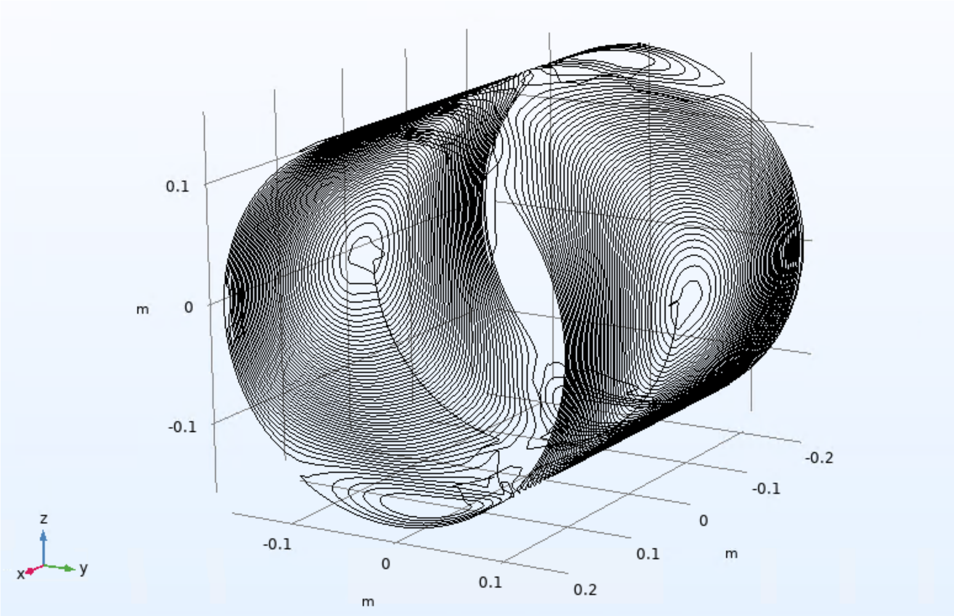

Figure 3.2: Coil for the Y-axis

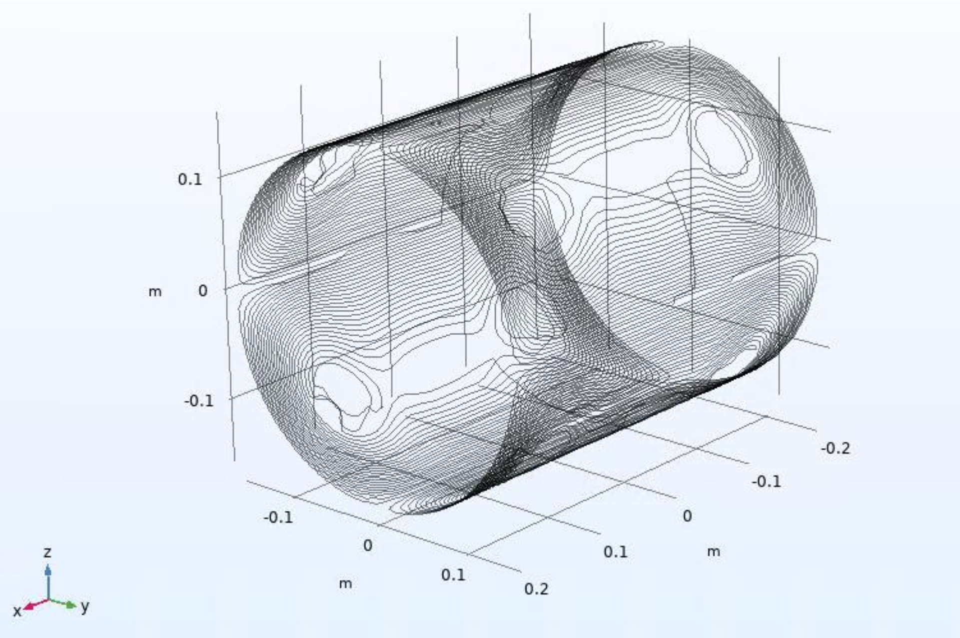

Figure 3.3: Coil for the Z-axis

3.2 Evaluation of magnetic field gradients

The resulting values measured by cutline were plotted in graphs, which you can see in Figures 3.1, 3.2 and 3.3. Each figure contains two graphs. The first is the result of a stationary study, and the second is a frequency domain study. Both studies made very similar results, so that is why one of them is harder to see.

In the table 3.1 shows the changes in magnetic induction from the beginning of cutline to the middle (0.125 m) due to the symmetry of the graph. However, in the center is not exactly zero, so it is necessary to calculate the change more precisely. The change was calculated by subtracting the value at the center from the value at the beginning. Then the table shows magnetic field gradient calculated by using the formula 2.1. For X-axis coil gradient, the result is 5.84 mT/m. For Y-axis coil, the result of gradient is 28.97 mT/m. The gradient for Z-axis coil is 18.69 mT/m. The last information shown in the table is the length of the conductors which was measured in COMSOL.

Table 3.1: The resulting values of change in magnetic induction and the gradients of the resulting field.

Coil	Change in magnetic induction (mT)	Magnetic field gradient (mT/m)	Length of the conductor (m)
X-axis	0.73	5.84	62.14
Y-axis	3.25	25.97	89.04
Z-axis	2.33	18.69	98.05

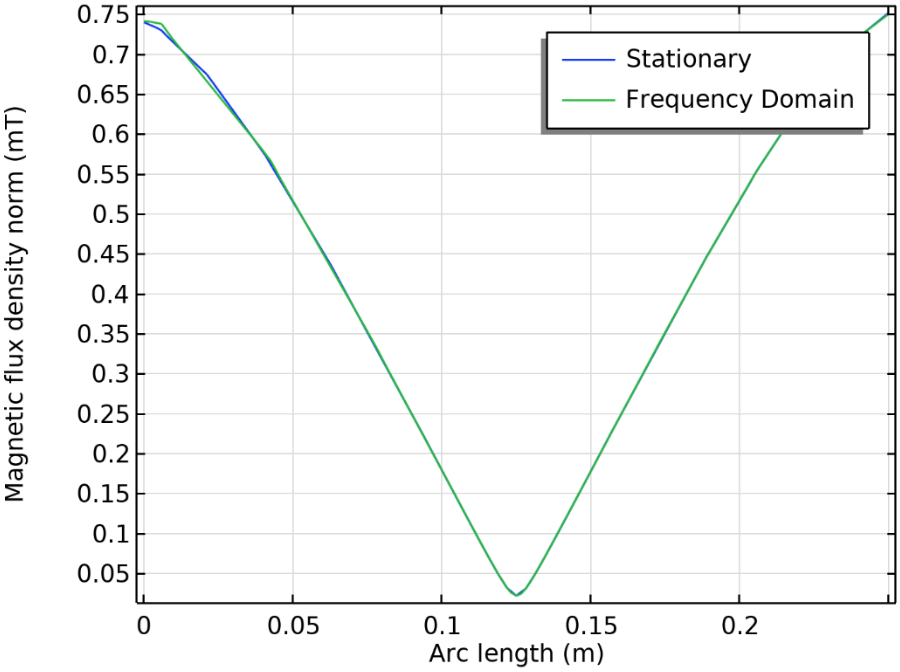

Figure 3.1: Magnetic field changes for the X-axis coil

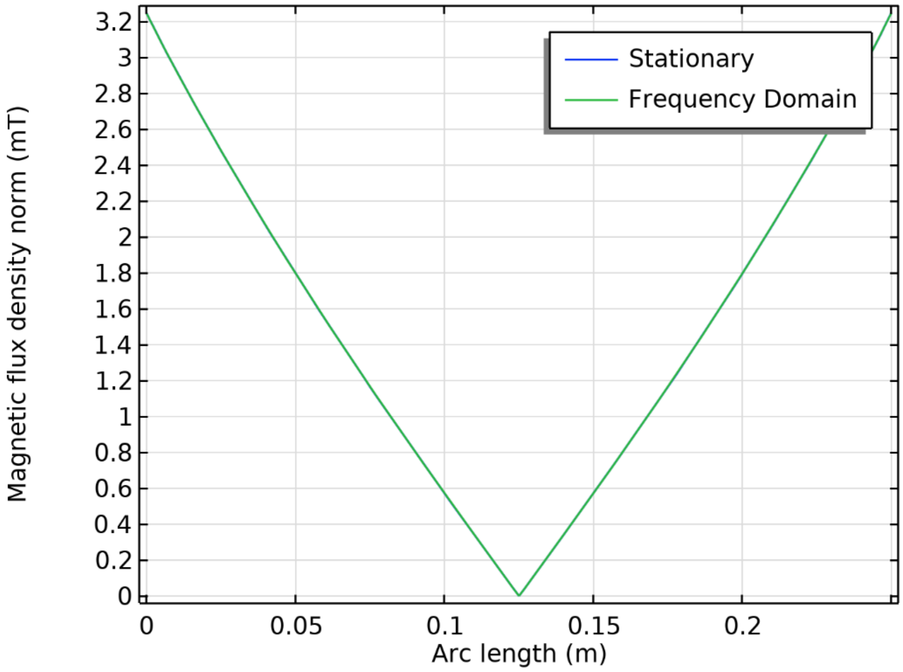

Figure 3.2: Magnetic field changes for the Y-axis coil

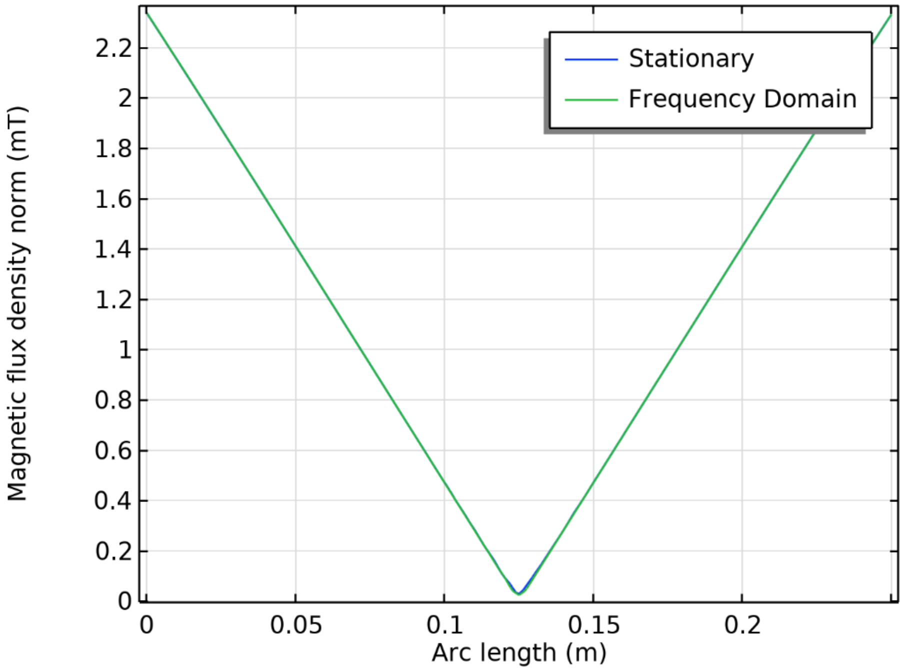

Figure 3.3: Magnetic field changes for the Z-axis coil

3.3 Production and measurement of the gradient coil for the Y-axis

The figure 3.4 shows a physically wound coil. The coil was measured using the four-terminal method, which measured a coil resistance of 1.05 Ω at a current of 9.3 A.

Subsequently, the measurement was performed using an RLC meter (Agilent 4284A) at an alternating current frequency of 10 kHz. The inductance of the coil was measured at 567.2 µH and its resistance at 0.768 Ω.

Resulting change in magnetic induction was 1.6 mT and the resulting gradient was 12.8 mT/m.

Figure 3.4: Executed gradient coil for the Y axis

4. DISCUSSION

Only one measuring cutline is always guided by center of the specific coil model, as we are mainly interested in the linearity of the main axis of the given coil's gradient. The entire cutline is just located in a spherical target field so it can precisely measure resulting gradient.

As you can notice, the difference between results of stationary and frequency domain is not visible in figure 3.1, 3.2 and 3.3. This is caused by the material not being assigned to the conductor. The reason for this is the creation of the coil geometry itself by using an interpolation curve, to which material cannot be assigned without using the sweep function, i.e., extension. For such a complex structure as these coil models, it was not possible to use the sweep function. Thus the current is not creating any eddy currents, skin effect or even frequency dependence in the simulation. It caused the results of the stationary study equivalent to those of the frequency domain study.

The length of the conductor is mainly influenced by the number of loops, which also plays a key role in the correct and desired functionality of the coil. The selected number of loops is primarily used to achieve the required gradient strength. Since the gradient strength of some coils is several times greater than required, i.e., 5 mT/m, it can be optimized in further work.

During the physical winding of coil Y, the required length of the conductor was measured incorrectly, so it was necessary to connect the conductor by soldering a wire. Despite this connection, we obtained a resistance of 1.05 Ω using method of four-terminal connections and 0.77 Ω when measuring with an RLC meter, which indicates a successful connection.

5. CONCLUSION

The aim of this project was to create a system of conventional gradient coils for changing the magnetic field, i.e. for creating a linear gradient. The diameter of the narrowest coil was set at 290 mm, and the length of the system was 420 mm. The gradient of the resulting magnetic field meets the minimum limit of 5 mT/m in all three models at a current of 15 amps. Specifically, for the X coil it is 5.84 mT/m, for the Y coil it is 25.97 mT/m, and for the Z coil it is 18.69 mT/m. The lengths of the conductors of the individual coils are mentioned in chapter 3.2 Evaluation of magnetic field gradients. According to figures 3.1, 3.2 and 3.3, the requirement to achieve a linear gradient field in the target field was met.

Beyond the aim of the work, a coil for the Y-axis was physically realized. Its resistance was measured using the four-terminal method with a current of 9.3 A flowing through it. Using this method, its resistance was measured to be 1.05 Ω. Furthermore, its resistance and inductance were also measured using an RLC meter. The resistance was 0.77 Ω and the inductance was 567.2 μH. The final measurement was performed using a teslameter, which told us that the resulting gradient was 12.8 mT/m in the main Y-axis.

ACKNOWLEDGMENT

I would like to thank my supervisor, Professor David Vrba, for his valuable advice and patience. I would also like to thank Ing. Matouš Brunát for his useful advice.

REFERENCES

[1] *Medical devices: magnetic resonance imaging units (per million population), total density* [online]. [vid. 2025-06-11]. Dostupné z: https://www.who.int/data/gho/data/indicators/indicator-details/GHO/total-density-per-million-population-magnetic-resonance-imaging

[2] HORI, Masaaki, Akifumi HAGIWARA, Masami GOTO, Akihiko WADA a Shigeki AOKI. Low-Field Magnetic Resonance Imaging-Its History and Renaissance. *Investigative Radiology* [online]. 2021, **56**(11), 669–679 [vid. 2024-10-05]. ISSN 0020-9996. Dostupné z: doi:10.1097/RLI.0000000000000810

[3] *A4IM - A4IM* [online]. [vid. 2025-09-04]. Dostupné z: https://www.a4im.ptb.de/home